Structural and Multidisciplinary Optimization (2020) 61:319–341
https://doi.org/10.1007/s00158-019-02362-z

RESEARCH PAPER

Shape optimization of underwater wings with a new multi-fidelity bi-level strategy

Siqing Sun[1] · Baowei Song[1] · Peng Wang[1] · Huachao Dong[1] · Xiao Chen[1]

Received: 5 December 2018 / Revised: 1 July 2019 / Accepted: 15 July 2019 / Published online: 14 August 2019

Abstract

This paper proposes a new multi-fidelity bi-level optimization (MFBLO) strategy for shape designs of underwater wings. Firstly, hydrodynamic analyses of the wing planform and sections are decoupled for constructing a bi-level shape optimization frame, which includes an upper-level task merely concerning the wing planform design and several lower-level tasks only related to the section designs. By doing this, the shape design optimization gets remarkable benefits from the reduction of dimension and computational costs. Secondly, the bridge function method combined with three multi-fidelity data fusion approaches CC1, CC2, and CC3 are proposed to conduct the bi-level optimization, respectively. After comparison analyses, CC2 shows higher computational efficiency and accuracy, which is more appropriate for the bi-level shape optimization frame. Finally, compared with the single-level optimization with the fixed planform or sections and the conventional high-dimensional optimization, the proposed MFBLO needs less computation budget and gets higher lift-drag ratio, showing its outstanding advantages in handling the shape optimization of underwater wings.

Keywords High-dimensional expensive problem · Bi-level optimization · Multi-fidelity surrogate models · Underwater wing design

Nomenclature of important variables

Subscripts

u, l	Upper and lower
i, j	Indexes
_	Separator

Superscripts

*	Optimal values

Symbols

b	Wing span,
c_r, c_t	Root and tip chords
λ	Leading edge angle
S_w	Planform area
ns	Number of sections
n	Dimension of problems
V	Velocity
α	Angle of attack (AOA)
F, f, G, g, H, h, x	Objective functions, constraints and design variables of bi-level optimizations
ind, eff	Induced and effective,
prof,∞	Profile and far field
HF, LF	High and low fidelities
^	Predicted values
c, t/c	Chord, relative thickness of sections
Sp	Spanwise position of sections
w_{li_j}	jth Parameter of ith section shape curve function
ind$V$	Induced velocities in VLM
w	Area weight coefficients
N	Looping index of optimizations
L, D, C_L, C_D	Lift, drag, and their coefficients of UWs
l, d, C_l, C_d	Lift, drag, and their coefficients of sections

Responsible Editor: Hai Huang

Electronic supplementary material The online version of this article (https://doi.org/10.1007/s00158-019-02362-z) contains supplementary material, which is available to authorized users.

✉ Peng Wang
wangpeng305@nwpu.edu.cn

[1] School of Marine Science and Technology, Northwestern Polytechnical University, Xi'an 710072, China

1 Introduction

Different from traditional autonomous underwater vehicles, underwater gliders usually have a pair of wings to improve the hydrodynamic performance (Rudnick 2016; Javaid et al. 2014). Hence, it is essential and significant to design and optimize underwater wings (UWs) (Luo and Lyu 2015). Generally, the geometry parameters of UWs consist of two parts: the wing planform and sections, where the planform involves 4–15 variables and each section includes 10–12 variables. Thus, a complete UW shape may be composed of hundreds of design variables, which belongs to high-dimensional design problems (Koo and Zingg 2017). On the other hand, accurate hydrodynamic analyses by CFD simulations (averagely 30–60 min) are computationally intensive (Oberkampf and Trucano 2002), also bringing another challenge for optimization (Lyu et al. 2014). For the abovementioned high-dimension expensive problem, a large number of sampling points are required to identify its optimal solutions, which generate unbearable computational cost, also known as "curse-of-dimensionality" (Koch et al. 1999).

In the past two decades, many modeling and optimization methods were presented, but most of them are limited to low-dimensional problems (Wang et al. 2004; Regis 2015). To solve high-dimensional expensive optimization problems, some strategies try to turn high dimensionality into low dimensionality (Viswanath and Asha 2010; Harrington and Gorder 2015; Hartwig and Bestle 2017), mainly including mapping, screening, and decomposition (Shan and Wang 2010). Mapping exploits implicit relations between the design variables and translates them into uncorrelated and fewer variables. Meanwhile, most of the original information are remained (Li and Chen 2006; Bohn et al. 2016). However, the new and the original optima may be different owing to the change of the design space. Screening discriminates and ignores less relevant variables to reduce the dimension (Harada et al. 2006; Zhang 2014), while the dimension may still be high for problems with many equally important design variables. In a word, mapping and screening concentrate on relation among variables or importance of variables to the function, whereas decomposition pays more attention to intrinsic characteristics of the function. With the help of decomposition, the original problem can be divided into a series of smaller scale sub-problems according to their physical features (Yata and Aoshima 2010; Moritz et al. 2016).

Decomposition has a lot of advantages in dealing with high-dimensional expensive optimization problems, including the reduction of sub-problem dimensionality, the improvement of efficiency with parallel abilities, the compatibility of different solution techniques, and the support of multi-criteria analyses (Yang et al. 2018; Mei et al. 2016). However, its application is strongly restricted by the problem decomposability. To the best of our knowledge, there are fewer decomposition methods for solving the Navier-Stokes equations so far. Thus, in our work, another hydrodynamic solver named quasi-three-dimensional (Q3D) is adopted to meet the usage condition of decomposition (Mariens et al. 2014; Graf et al. 2014). The solver decouples the wing planform and section analyses according to the unique fluid phenomenon of UWs. Specifically, section analyses are totally independent with each other and are weakly coupled with the planform analysis. This relation indicates the stratified nature of the problem (Mitsos et al. 2009; Sinha et al. 2018), where the planform design is an upper-level (UL) optimization problem and each section design is a lower-level (LL) optimization problem. Therefore, the specific high-dimensional expensive UW design problem is now decomposed into many low-dimensional expensive sub-problems cooperating with each other in the bi-level form.

Although the dimension is reduced, the nested structure brings quite a number of LL optimization tasks. Thus, in view that each task is an expensive problem, the total computational burden is still heavy. Fortunately, the computational cost can be dramatically decreased by surrogate models (SMs) (Jones et al. 1998; Simpson et al. 2001), also called "response surfaces," "meta-models," or "approximation models." As the name suggests, SM is a cheap approximate model constructed by a certain amount of samples and their true responses. It can be used to efficiently predict values at any untried points. Hence, the expensive function evaluation is avoided to reduce the burden. However, a few samples cannot guarantee the accuracy of SMs, while massive sample data will bring huge computation cost. Hence, multi-fidelity models (MFMs) are adopted to further improve the efficiency, which are constructed by a few expensive high-fidelity (HF) data and more low-fidelity (LF) data (Nguyen et al. 2013; Huang et al. 2015; Leifsson and Koziel 2015). Despite the wide application of MFMs, there are fewer literatures about constructing MFM in a bi-level optimization flow. Besides, this brings some additional conundrums, which are mainly caused by how to combine LF and HF data of each optimization level. On one hand, the response value of each level should be accurate enough and sensitive to all design variables. On the other hand, the whole optimization process should be fast and the MFM should be robust enough under thousands of function evaluations.

To make up this research gap, we propose three different multi-fidelity data fusion approaches CC1, CC2, and CC3, and CC2 performs the best on the engineering tests. CC2 uses LF data in LL optimization completely, while MFM is built in UL optimization to modify the accuracy. Hence, CC2 is recommended to be used in the proposed multi-fidelity bi-level optimization (MFBLO) strategy to maximize the Lift-to-Drag ratio (L/D) of UWs. Compared with the existing methods, the new optimization strategy has the following contributions:

- A nested bi-level optimization frame is built for the shape optimization of UWs to reduce optimization dimension and computational cost.

- Three multi-fidelity modeling approaches for nested optimizations are constructed to improve accuracies and computational efficiency, where CC1 combines LF and HF data in LL optimization, CC2 is constructed in the UL, while CC3 is built in both levels.
- MFBLO is not only applicable for the design of UWs but also can be extended for other hierarchical optimal design problems with multiple fidelity data, such as structural optimization (Ragon et al. 2015), designs of transportation (Wang et al. 2018), and electrical networks (Quashie et al. 2018).

2 Bi-level shape optimization frame

Before decomposing the shape problem, it is necessary to introduce the details of the proposed bi-level optimization frame. As (1) shows (Islam et al. 2017), the nested optimization tasks are consisted of two levels, namely UL and LL, which have their own design variables, constrains, and objective functions. For LL, the objective function is optimized with respect to the LL variables, whereas the UL variables act as fixed parameters. For UL, the objective function is optimized with respect to the UL variables with the corresponding optimal LL solution. Thus, the bi-level optimization problem aims at determining the optimum of UL and meanwhile satisfying the optimality of LL.

$$\begin{aligned} &Min \quad F_u(x_u, x_l) \\ &W.r.t \quad x_u \in X_U, x_l \in X_L \\ &S.t \quad G_k(x_u, x_l) \le 0, k = 1, \ldots q_u \\ &\quad H_k(x_u, x_l) = 0, k = 1, \ldots r_u \\ &\quad \begin{cases} x_l \in \underset{x_l \in X_L}{\operatorname{argmin}} \{ f_l(x_u, x_l) \} \\ g_k(x_u, x_l) \le 0, k = 1, \ldots q_l \quad h_k(x_u, x_l) = 0, k = 1, \ldots r_l \end{cases} \end{aligned} \tag{1}$$

where the subscripts u and l refer to UL and LL, respectively. Correspondingly, $F_u(x_u, x_l)$ is the UL objective function and $f_l(x_u, x_l)$ is the LL objective function. The UL design vector x_u is in domain X_U, and the LL design vector x_l has its domain X_L. G and H are the sets of q_u inequality and r_u equality constrains for UL. Accordingly, g and h represent inequality and equality constrains in LL, respectively.

The total parameters of an UW shape come from the planform and sections, as shown in Table 1 and Fig. 1. All the planform parameters are independent. The shape curve variables in the section parameters are also independent, while other section parameters such as the chord and the thickness are determined by the planform geometry. Hence, the two groups of parameters can be divided into two categories, in which the planform variables belong to UL and section variables belong to LL. Thus, the original high-dimensional vector is reasonably transformed into the bi-level format, and each optimization task has fewer design variables. On the other hand, hydrodynamic analyses are needed to provide the objective functions. More importantly, hydrodynamic analyses of the planform and sections must be separated according to the decomposition method of the design variables. Thus, Q3D that is a similar, semi, or approximate 3D method is applied to achieve the goal. The basic theory of Q3D is introduced, and a bi-level optimization model for UWs is constructed correspondingly.

2.1 Quasi-three-dimensional hydrodynamic solver

The Q3D hydrodynamic solver is specially developed to predict the lift and drag of UWs under low Reynolds values. As Fig. 2 shows, V_∞ and α are the velocity and the angle of attack (AOA) of the far-field incoming flow, respectively. According to the finite wing phenomenon, the effective incoming flow of each section is different, including the effective velocity V_{eff_i} and the effective AOA α_{eff_i}. The approach uses the planform analysis to calculate the effective incoming flow of each section, and hydrodynamic data of each section are obtained by section analyses according to the effective flow. Finally, the solver integrates the hydrodynamic data of each section according to the planform geometry to gain the results. Obviously, the planform analysis and section analyses are separated, and the main procedure is briefly explained as follows:

1) Input phase: The shape and flow field parameters are given by users, and then the geometry model of an UW is constructed according to the inside parametric method.
2) The vorticity distribution: The vortex lattice method (VLM) is employed to calculate the vorticity distribution among the planform. The wing is modeled as a set of lifting panels according to the thin hydrofoil theory. The horseshoe vortices and control points are placed on each panel under the "1/4–3/4" chord position rules, as shown

Table 1 Wing geometric parameters

	Wing planform				Sections number	ith hydrofoil		
Parameter	Wing span	Wing root	Leading edge angle	Wing tip		Spanwise position	Relative thickness	Shape curve
Symbol	b	c_r	λ	c_t	ns	$Sp_i = [(i-1)b]/[2(n-1)]$	$(t/c)_i$	w_{li_j}

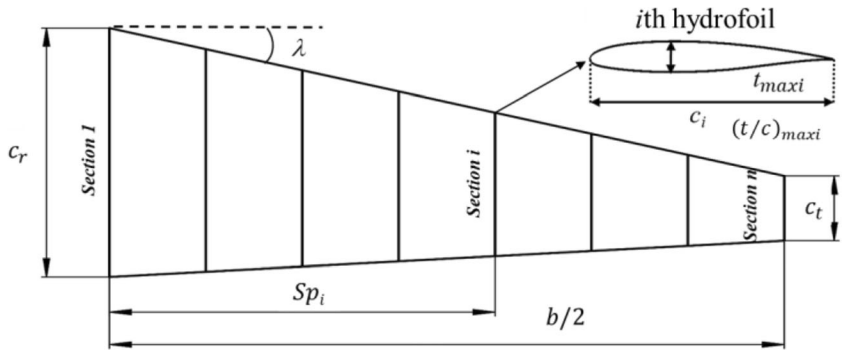

Fig. 1 Illustration of wing geometric parameters

in Fig. 3. The Biot-Savart's law is used to calculate the induced velocity indV_i generated by horseshoe vortices, and the Neumann boundary condition of no penetration is enforced at the control points. Hence, (2–3) are listed, and the Gauss-Seidel method is used to solve them, for obtaining the vorticity Γ_j on each board.

$$indV_i = \sum_{j=1}^{N} A_{i\,j} \cdot \Gamma_j \tag{2}$$

$$V_\infty \cdot \sin(\alpha) + indV_i = 0 \tag{3}$$

where the influence coefficient A_{ij} represents the induced flow on the ith panel control point due to the vortex on jth panel, and it is determined by the position difference between the ith point and jth vortex.

3) The downwash angle of each section: The downwash angle of each section $\alpha_{\text{ind\_i}}$ is influenced by wing-tips' vortices, and it is obtained with (4) after determining the vorticity distribution.

$$\alpha_{\text{ind\_i}} = \frac{1}{4\pi V_\infty} \int_{-b/2}^{b/2} \frac{d\Gamma_\zeta / d\zeta}{z - \zeta} d\zeta \tag{4}$$

where b is the span-wise length of an UW, and z is span-wise position of the current hydrofoil, while ζ is span-wise position of the vortex filament Γ_ζ.

4) The effective incoming flow span-wise distribution: According to Fig. 2, (5–6) are set up to gain the effective incoming flow of each section. The induced drag D_{ind} is calculated based on the Trefftz plan analysis, as shown in (7).

$$\alpha_{\text{eff\_i}} = \alpha - \alpha_{\text{ind\_i}} \tag{5}$$

$$V_{\text{eff\_i}} = V_\infty / \cos(\alpha_{\text{ind\_i}}) \tag{6}$$

$$D_{\text{ind}} = \rho V_\infty \int_{-b/2}^{b/2} \Gamma_\zeta \cdot \alpha_{\text{ind\_i}} \cdot d\zeta \tag{7}$$

From steps 2 to 4, there is no equation requiring the section shape information. Only the planform and the far-field flow parameters are needed. Hence, these steps are regarded as wing planform analysis phase one.

5) Flow analyses of 2D sections: Reynolds average Navier-Stokes (RANS) methods are adopted to solve the flow field of sections. As a result, the effective lift $l_{\text{eff\_i}}$ normal to $V_{\text{eff\_i}}$ and the effective drag $d_{\text{eff\_i}}$ parallel to $V_{\text{eff\_i}}$ are obtained, as Fig. 2 shows.
6) Force relation analyses: In Fig. 2, F is the total hydrodynamic force. Using the force relationship, the far-field lift l_{∞_i} normal to V_∞ and the far-field drag d_{∞_i} parallel to V_∞ are calculated according to (8–9).

$$l_{\infty\_i} = l_{\text{eff\_i}} \cos(\alpha_{\text{ind\_i}}) - d_{\text{eff\_i}} \sin(\alpha_{\text{ind\_i}}) \tag{8}$$

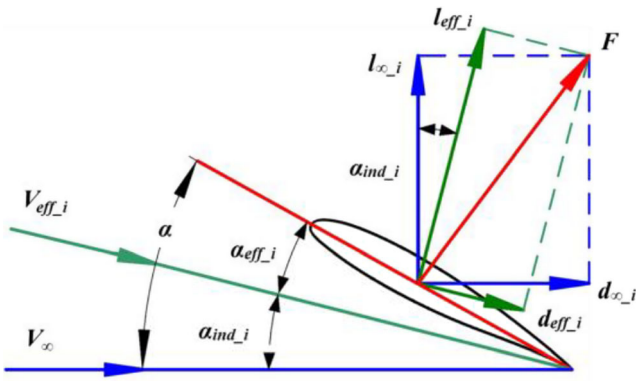

Fig. 2 Forces and angles of a hydrofoil

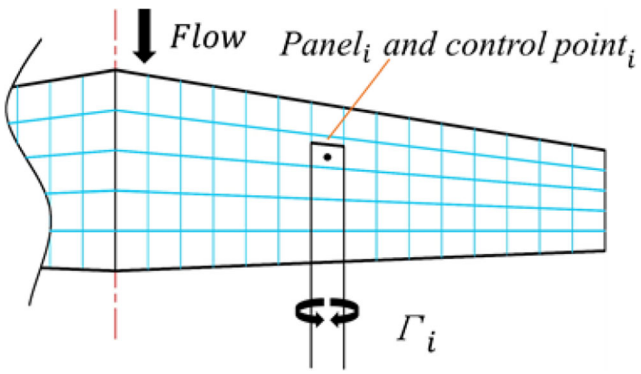

Fig. 3 Schematic of a single horseshoe vortex and control point

$$d_{\infty\_i} = d_{\text{eff\_i}}\cos(\alpha_{\text{ind\_i}}) + l_{\text{eff\_i}}\sin(\alpha_{\text{ind\_i}}) \tag{9}$$

From steps 5 to 6, there is no equation requiring shape information of the wing planform. Hence, these steps are regarded as wing section analyses, and each section analysis is an independent process.

7) The lift calculation: The lift coefficient C_L of the 3D UW is obtained by integrating the far-field lift coefficient $C_{l\infty\_i}$ of each section.

$$C_L = \frac{2}{S_w}\int_0^{b/2} C_{l_{\infty\_i}} c_i dy \tag{10}$$

where c_i is the chord of the current section. S_w and dy represent the wing planform area and a tiny length on span-wise, respectively.

8) Drag calculation: In (9), the first item is the profile drag $d_{\text{prof\_i}}$, and the second refers to the induced drag $d_{\text{ind\_i}}$. However, the induced drag is not considered here, because it is predicted more accurately by (7), which uses the far-field analysis method. Thus, only the total profile drag coefficient $C_{D\text{prof}}$ is gained by integrating the profile drag coefficient $Cd_{\text{prof\_i}}$ using (11). Finally, the total drag coefficient of the UW is the sum of the profile drag and the induced drag, as shown in (12).

$$C_{D_{\text{prof}}} = \frac{2}{S_w}\int_0^{b/2} C_{d_{\text{prof\_i}}} c_i dy \tag{11}$$

$$C_D = C_{D_{\text{prof}}} + C_{D_{\text{ind}}} \tag{12}$$

Similarly, steps 7 to 8 are regarded as wing planform analysis phase two.

The lift and drag of an UW can be obtained by wing planform analysis phase one, wing section analyses, and wing planform analysis phase two. Specifically, the proposed Q3D working flow is shown in Fig. 4.

2.2 Mathematical model of the bi-level shape optimization

2.2.1 The UL optimization frame

The UL optimization is the leader level, responsible for the overall hydrodynamic performance. Generally, the maximum L/D is considered as the goal of the shape optimization, and it is also regarded as the objective function of the UL optimization, expressed by (13). The lift and drag of an UW can be gained by (10–12) and (14–15) provide the corresponding discrete formats.

$$F_u(x_u, x_l) = C_L/C_D \tag{13}$$

$$C_L = \sum_{i=1}^{ns} w_i C_{l_{\infty\_i}} \tag{14}$$

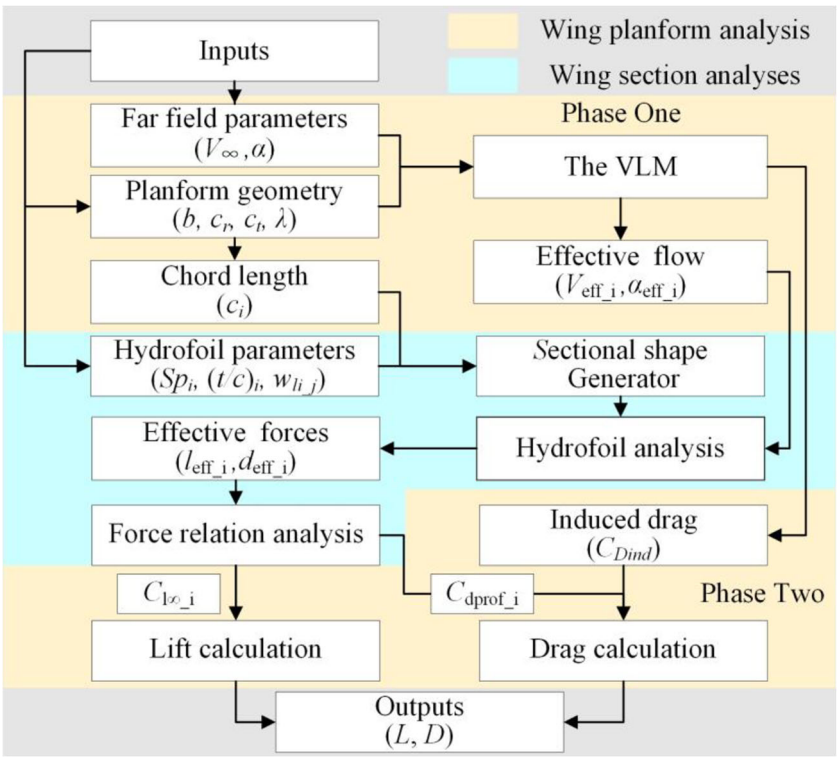

Fig. 4 Q3D hydrodynamic solver

$$C_D = \sum_{i=1}^{ns} w_i C_{d\text{prof\_i}} + C_{D\text{ind}} \tag{15}$$

where w_i is the area weight coefficient of ith section, determined by the planform geometry, as shown in (16–17):

$$width = b/(2{\cdot}ns) \tag{16}$$

$$w_i = \begin{cases} \left(\frac{3}{4}{\cdot}c_1 + \frac{1}{4}{\cdot}c_2\right){\cdot}\frac{width}{S_w} & i = 1; \\ 2{\cdot}c_i{\cdot}width/S_w & i = 2, 3...(ns{-}1); \\ \left(\frac{3}{4}{\cdot}c_{ns} + \frac{1}{4}{\cdot}c_{ns-1}\right){\cdot}\frac{width}{S_w} & i = ns; \end{cases} \tag{17}$$

where ns is the number of wing sections, and this paper selects eight sections in equidistant span-wise distance (Mariens et al. 2014). width is the span-wise distance between two selected sections, and S_w is the total area of the wing planform. Thus, w_i is regarded as a simple function only related with the planform parameters.

It seems that the objective function is with respect to many variables, including $C_{l\infty\_i}$, $C_{d\text{prof}\_i}$, and $C_{D\text{ind}}$, the planform parameters and the far-field parameters. Among them, the far-field parameters are constants in the optimization process. To write the objective function into a compound function only related to the planform parameters, analyses are needed to prove that $C_{l\infty\_i}$, $C_{d\text{prof}\_i}$ and $C_{D\text{ind}}$ are direct or indirect functions of the planform parameters, and Fig. 5 shows the specific flow.

Firstly, for the direct relations, $C_{D\text{ind}}$ is gained by (7) in wing planform analysis phase 1. Hence, it is only influenced by the planform geometry and the far-field parameters.

Secondly, for the indirect relations, $C_{l\infty\_i}$ and $C_{d\text{prof}\_i}$ are calculated by the effective incoming flow and ith section shape. Among them, the effective incoming flow is a function of the wing planform parameters. Though ith section shape is not determined in the UL, its variable range is known. Hence, the optimal $C_{l\infty\_i}^*$ and $C_{d\text{prof}\_i}^*$ can be found by LL optimizations. Thus, $C_{l\infty\_i}^*$ and $C_{d\text{prof}\_i}^*$ are implicit functions of the planform parameters, and they are counted as intermediate variables (IVs*) here.

Finally, the UL object function can be expressed as an operation of the wing planform parameters and some output IVs* from section analyses, and the optimization formula is presented as follows.

$$\begin{aligned} Max \quad & F_u[g(x_u)] = \sum_{i=1}^{n} w_i C_{l\infty\_i}^* \Big/ \left(\sum_{i=1}^{n} w_i C_{d\text{prof\_i}}^* + C_{D\text{ind}}\right) \\ & \left[w_i, C_{l\infty\_i}^*, C_{d\text{prof\_i}}^*, C_{D\text{ind}}\right] = g(x_u, x_l) \\ W.r.t \quad & x_u = [\,planform\ geometry\ parameters] \\ S.t \quad & constrains\ about\ planform\ geometry; \\ & x_u \in X_U; \quad x_l \in \underset{x_l \in X_L}{\operatorname{argmin}} \{\ f_l(x_u, x_l)\ \}; \end{aligned} \tag{18}$$

2.2.2 The LL optimization frame

The LL optimization is the follower level, in charge of the local hydrodynamic performance. Thus, the effective incoming flow is determined by the given planform geometry. LL optimizes the section shape for finding the hydrofoil with maximum $C_{l\infty\_i}/C_{d\infty\_i}$. Thereafter, IVs* including $C_{l\infty\_i}^*$ and $C_{d\text{prof}\_i}^*$ is calculated through the section analysis of the optimum shape and provided for UL. The ith LL optimization problem is defined as follows:

$$\begin{aligned} Max \quad & f_{l\_i} = C_{l\infty\text{\_i}}(x_{l\_i})/C_{d\infty\text{\_i}}(x_{l\_i}) \\ W.r.t \quad & x_{l\_i} = [\,ith\ hydrofoil\ parameters] \\ S.t \quad & constrains\ about\ ith\ hydrofoil\ geometry \\ & x_{l\_i} \in X_{L\_i} \end{aligned} \tag{19}$$

The architecture of the bi-level optimization is shown in Fig. 6. In addition to the benefit of the dimension reduction, the LL optimization can be executed in parallel, which can further improve the efficiency. Besides, the complex 3D

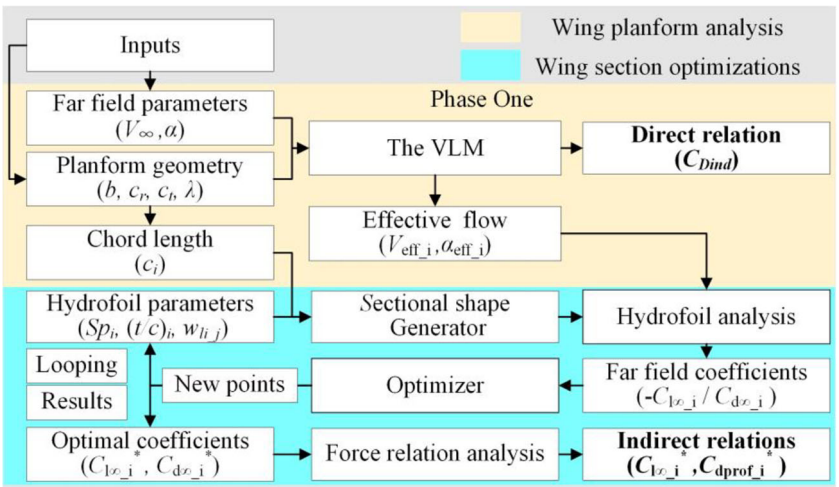

Fig. 5 Relations between $C_{l\infty\_i}$, $C_{d\text{prof}\_i}$ and the planform parameters

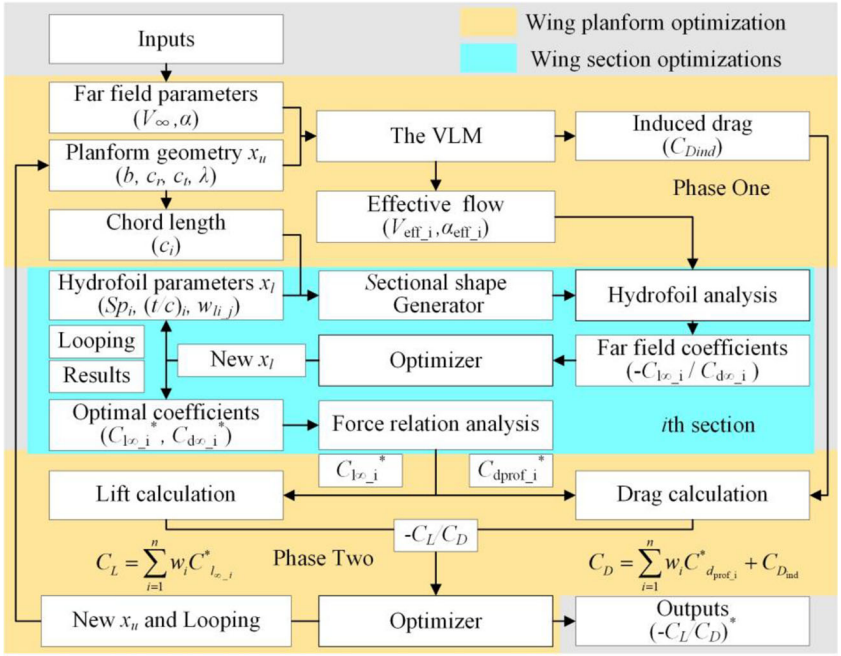

Fig. 6 The bi-level shape optimization frame

RANS simulation is replaced by simpler and faster 2D hydrofoil analyses, saving more computation source.

3 Multi-fidelity bi-level shape optimization frame

It seems that the proposed bi-level optimization can be easily realized by some traditional methods, such as heuristic algorithms or surrogate-assisted optimization methods. However, the optimization neglects the influence on the effective incoming flow distribution owing to changes of sections, which may reduce the accuracy. Moreover, different from conventional problems, the nested feature brings other challenges, especially in the following aspects:

- Though UL is a simple mathematical formula, it is still a NP hard problem for the bi-level structure, and it is difficult to converge (Jeroslow 1985).
- It is time-consuming to get the global optima of LL, which are required for each function evaluation in UL.

It can be seen that most challenges are concentrated on the expensive section analyses and optimization in LL. Reducing the computation budget of section analyses is essential and significant. Hence, MFMs are proposed to keep the analysis precision and improve the computation efficiency.

3.1 Low-fidelity hydrodynamic solver

XFoil that is an interactive inviscid/viscous program for analyses and designs of airfoils (Drela and Giles 1987; Drela 1989) is used for the LF section analysis. It combines a linear vorticity stream function panel code and an integral boundary layer formulation and is able to get accurate results in low speed aerodynamics. Hence, XFoil can also predict relatively accurate hydrodynamic data of hydrofoils in water as long as the Reynolds number is inserted correctly, according to the similarity criterion (Molland et al. 2004). Besides, XFoil calculates transition with the e^N envelope method, and a proper NT is obtained by (20) presented by van Ingen (2008).

$$NT = -8.43 - 2.4\ln(T_u) \tag{20}$$

where T_u denotes the turbulence intensity, and NT is set as 2 in this work for water environment. This corresponds to a rough wing surface in a high turbulence intensity freestream. In summary, the operation processes are presented as follows:

1) The coordinate data of the section shapes are uploaded to XFoil.
2) Number of panels is inputted by users, and 201 panels are proposed in this study.
3) The Reynolds value, AOA, and NT are inserted according to the work condition.
4) The lift and the drag coefficients and the pressure distribution curve are obtained.

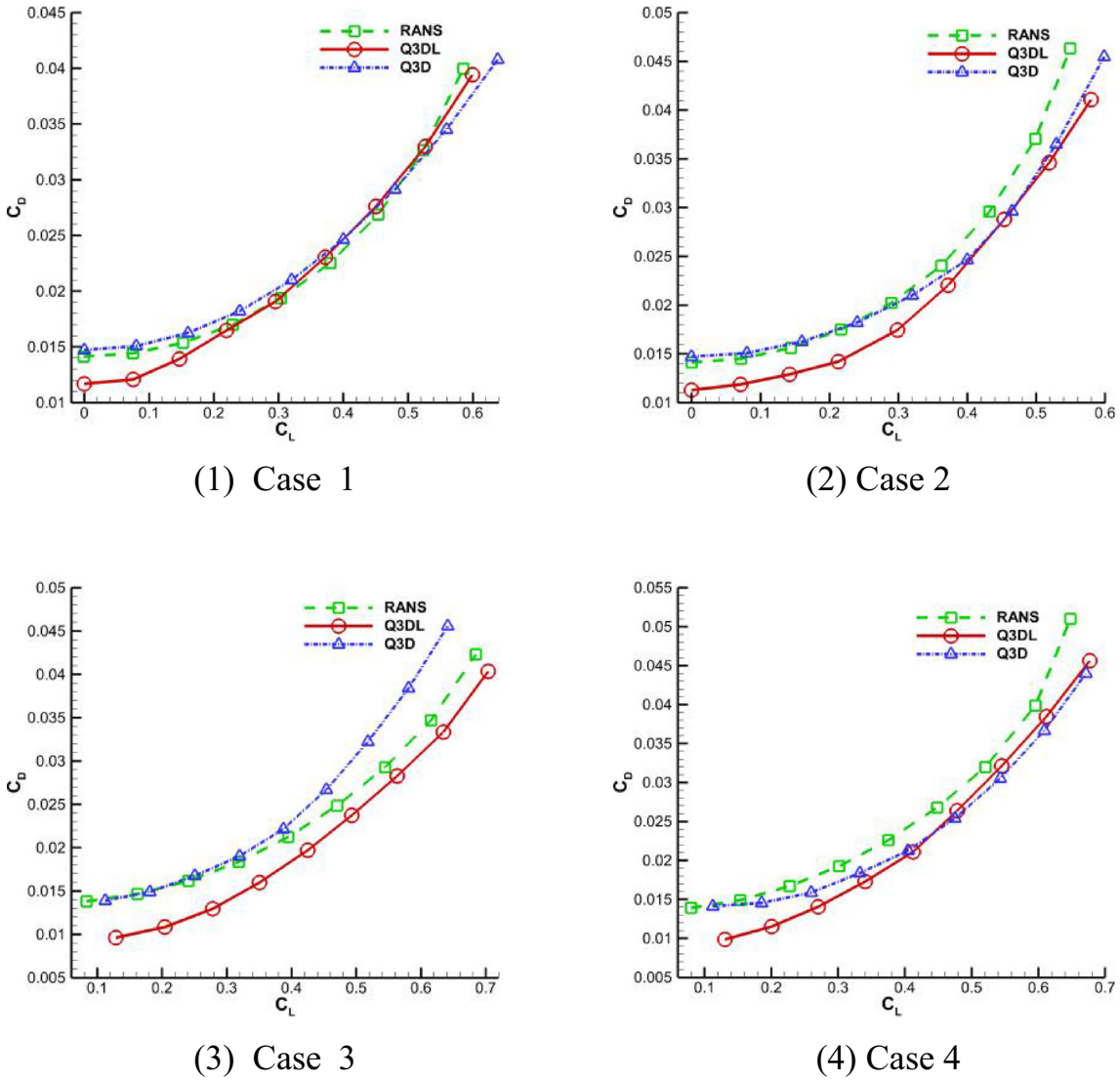

Fig. 7 Comparing results of Q3DL, Q3D, and RANS

The new solver for UWs is constructed by using XFoil in the section analyses, which is more rapid but has lower fidelity. The new solver is called Q3DL (Q3D in low-fidelity format), and it only costs about 4.5 s for calculating the hydrodynamics of an UW.

As Table 4 and Fig. 19 describe, 4 test cases under 9 working conditions are carried out to verify the effectiveness of Q3D, Q3DL, and 3D RANS, and results are listed in Fig. 7. These curves of the three results have a similar trend, which is the prerequisite for constructing MFMs. Thus, MFMs combining Q3DL and Q3D or RANS data can be used to acquire an accurate result at a reasonable cost.

3.2 Multi-fidelity theory

The core part of constructing a MFM is the way of combining the LF and HF data, and there are three popular methods, including the correction-based method, space mapping, and co-kriging (Li et al. 2018). The correction-based method is also called "bridge function," "scaling function," or "calibration," and it has simple structure and robust performance. The correction can be additive, multiplicative, or hybrid additive multiplicative, and the additive bridge function method is adopted here (Choi et al. 2004), and its general descriptions are as follows:

$$\hat{f}_{MFM}(x) = \hat{f}_{LFM}(x) + \hat{\gamma}(x) \tag{21}$$

$$\hat{\gamma}(x) = f_{HF}(x) - f_{LF}(x) \tag{22}$$

where $\hat{\gamma}(x)$ is the bridge function, and it is a SM built by the difference between LF and HF response data. MFM $\hat{f}_{MFM}(x)$ is the addition of LF SM $\hat{f}_{LFM}(x)$ and the bridge function $\hat{\gamma}(x)$.

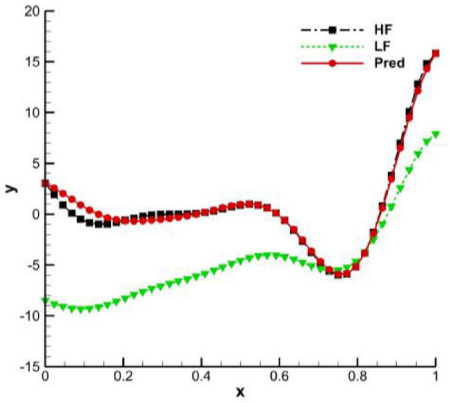

(1) Function curves of 1D

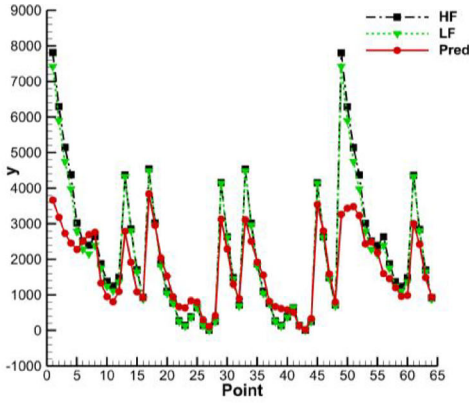

(3) Transformed function curves of 3D

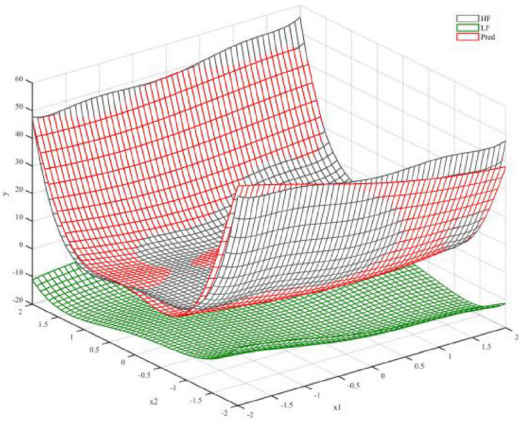

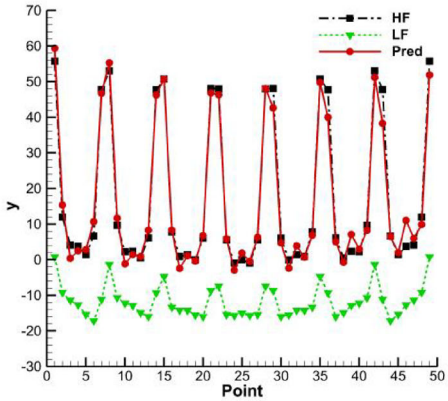

(2) Function graphs and transformed function curves of 2D

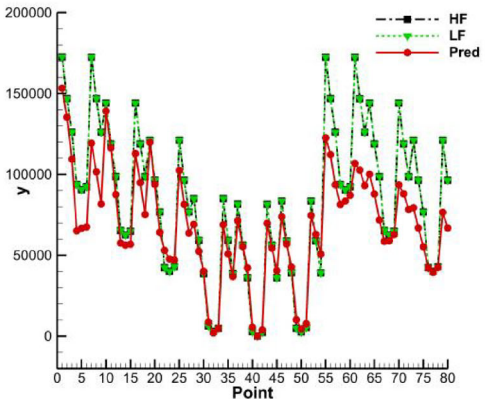

(4) Transformed function curves of 4D

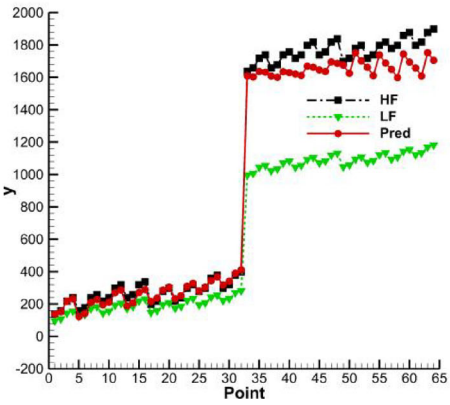

(5) Transformed function curves of 6D

Fig. 8 Results of tests of five mathematical examples

3.2.1 Tests on mathematical examples

It is important to determine the HF and LF data amounts for constructing MFMs. Obviously, the quantity of HF and LF data depends on the design dimension. Naturally, it is necessary to explore the relationship between data amount and dimension. For low-dimensional (≤ 2) problems, HF and MFM shapes can be captured from the function profiles, which can

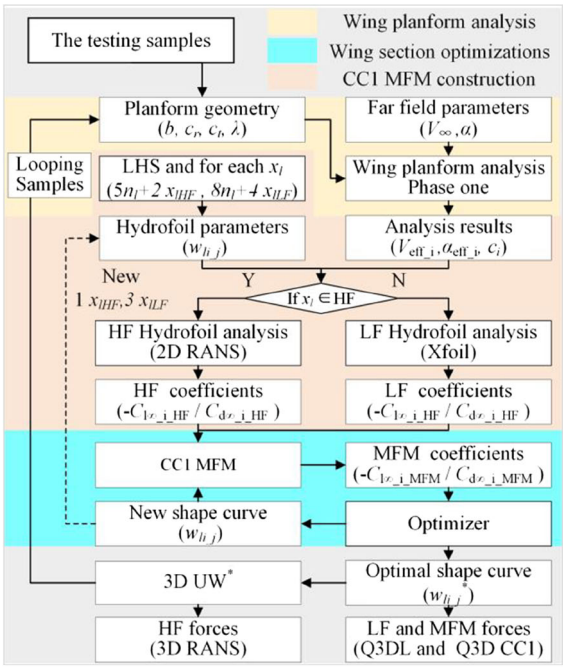

(1) Construction progress of CC1

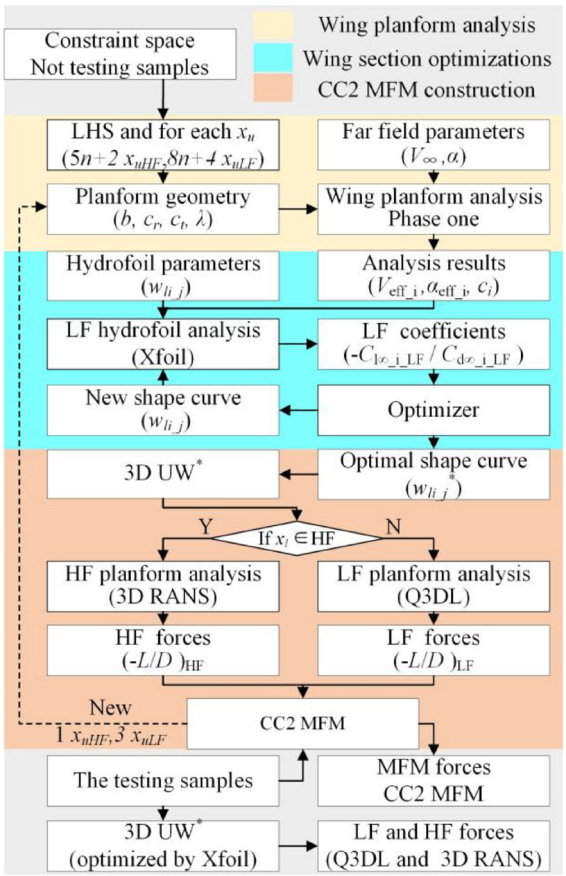

(2) Construction progress of CC2

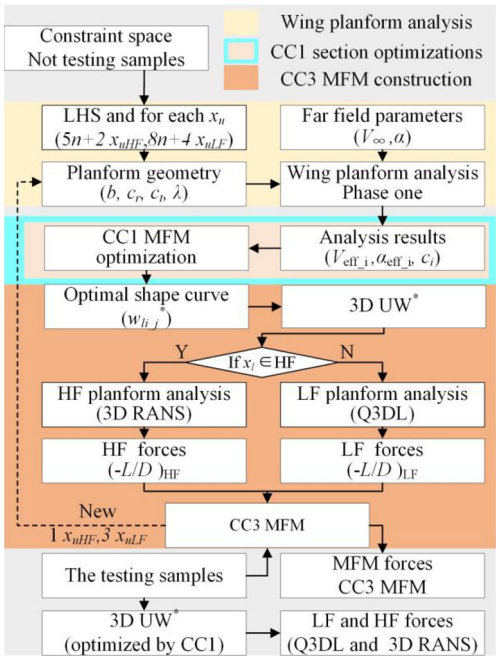

(3) Construction progress of CC3

Fig. 9 Testing progress of the MFMs

Fig. 9 (continued)

directly reflect the coincidence degree. For high-dimensional (> 2) problems, a one-dimensional curve is utilized to reflect the coincidence degree. Specifically, the curve is made up of the grid sampling points and the corresponding response values that are arranged in sequence.

Through tests on five different mathematical cases shown in Table 5 (Li et al. 2018), the relationship between the HF data amount m_{HF} and the dimension n is determined as $m_{\mathrm{HF}} = 5n + 2$, whereas the expression about the LF data amount m_{LF} and dimension is confirmed as $m_{\mathrm{LF}} = 8n + 4$, which is called the "$5n + 2$, $8n + 4$" rule in this paper. Results of tests on the five mathematical examples are shown in Fig. 8. The additive bridge function MFM has an excellent performance on the 1D, 2D, and 6D examples and is also able to capture the overall trend of 3D and 4D examples, which is good enough for the following optimization.

3.2.2 Multi-fidelity bi-level hydrodynamic solver

This part aims at combining LF and HF data to predict hydrodynamic data of the UW, which has the optimal sections at a given planform vector. As mentioned in Sect. 3.1 and Appendix 3, Q3DL is used to generate LF data. For HF data, there are two categories: One is the data obtained by Q3D adopting 2D RANS; the other one is the data calculated by 3D RANS. Hence, there are three multi-fidelity approaches to combine LF and HF data, named as CC1, CC2, and CC3.

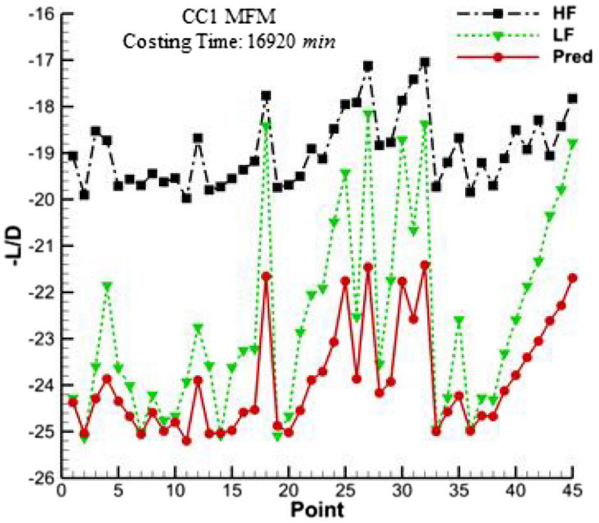

(1) Test results of CC1

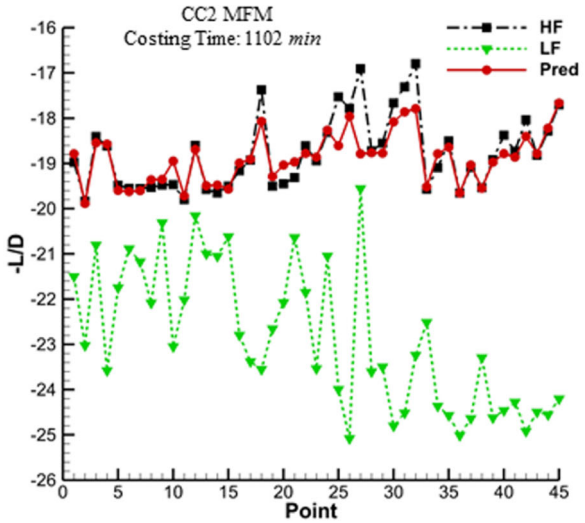

(2) Test results of CC2

Fig. 10 Test results of the MFMs

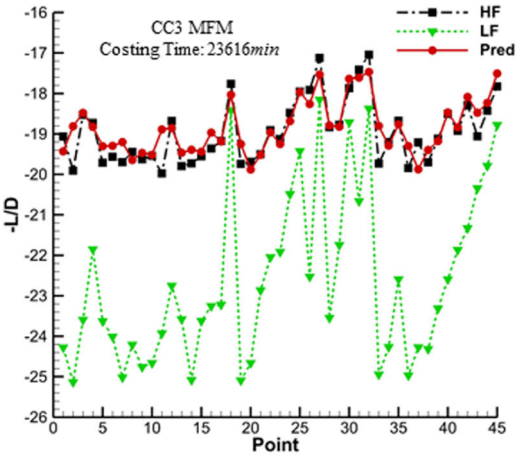

(3) Test results of CC3

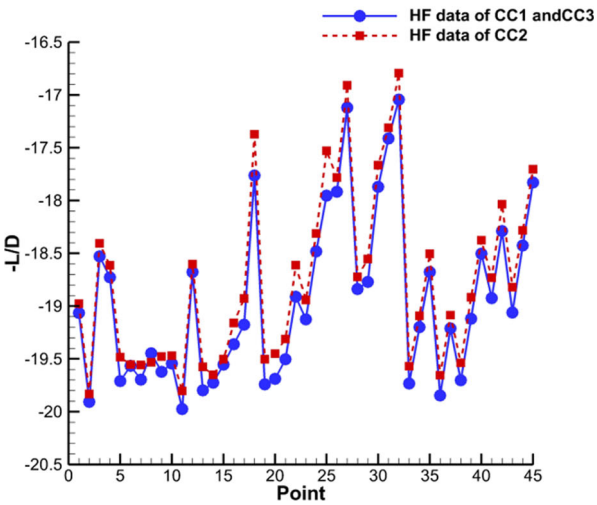

(4) Comparison results of HF data of the three MFMs

Fig. 10 (continued)

(1) As Fig. 9 (1) shows, CC1 combines data from XFoil and 2D RANS to construct MFM to predict hydrodynamic data of sections. Thereafter, section optimizations adopting MFM are carried out at the given vector to obtain the UW and its predictive hydrodynamic data.

Benefits are that data from XFoil and 2D RANS are very similar, helping to improve LL accuracy. However, CC1 also ignore the influence on the effective incoming flow distribution, which may reduce the precision. More importantly, computational costs of section analyses are hardly reduced.

(2) As Fig. 9 (2) shows, CC2 adopts XFoil in section optimizations at a few planform samples to obtain the optimal UWs. Subsequently, hydrodynamic data of the optimal UWs are calculated by Q3DL and 3D RANS to construct the MFM.

The advantage is that the accuracy is improved by the highest-fidelity 3D RANS data. However, CC2 lacks HF data in LL, which may be leading to a wrong optimization

Table 2 Performance indices of the MFMs

Six quantitative indices						
	1 Error E(|MFM-HF|)	2 Trend D(|MFM-HF|)	3 LL abilities ($-L/D$)	4 UL potential ($-L/D$)	5 Optimization capability ($-L/D$)	6 Costing time (min)
CC1	4.9614	0.3147	−18.9495	−19.9738	−19.9738	16920
CC2	0.2464	0.1712	−18.7824	−19.8321	−19.8321	1102
CC3	0.3317	0.1547	−18.9495	−19.9738	−19.6885	23616
Six normalized indices						
	1 Error	2 Trend	3 LL abilities	4 UL potential	5 Optimization capability	6 Costing time
CC1	1.0000	1.0000	0.9912	0.9929	0.9857	0.7165
CC2	0.0497	0.5442	1.0000	1.0000	0.9928	0.0466
CC3	0.0668	0.4915	0.9912	0.9929	1.0000	1.0000

direction. Furthermore, CC2 may be invalid due to the very complex relation between the planform vector and its optimal hydrodynamic data.

(3) As Fig. 9 (3) shows, CC3 employs CC1 to obtain the optimal predictive data at a few planform samples. Meanwhile, it combines the predictive and 3D RANS data to construct MFM, which is similar to CC2. Admittedly, this mode integrates the advantages of CC1 and CC2. However, the computing burden is also the summation of CC1 and CC2.

3.2.3 3.2.3 Performances of different MFMs

An engineering test is set up to compare the performances of different MFMs, and the flow charts are shown in Fig. 9. Far-field parameters are that V_∞ and α are 1 m/s and 4°, respectively. The testing samples are obtained by the grid sampling method used in the transformation curves. The dotted lines in Fig. 9 are not implemented here, because this part only concentrates on construction processes. The dotted lines represent the update of MFMs by one HF and three LF data, which will be adopted in optimization.

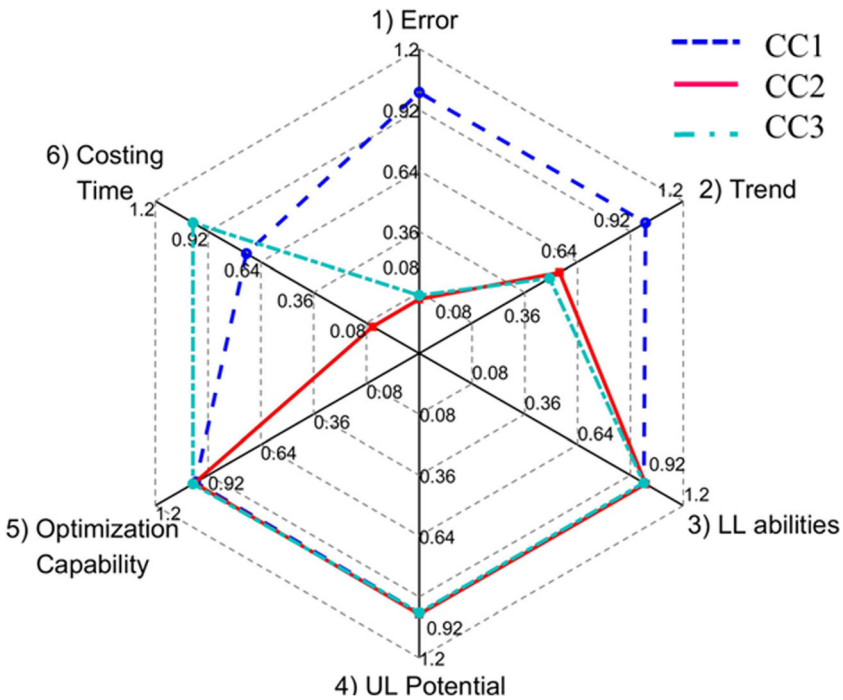

Fig. 11 Performances of different MFMs

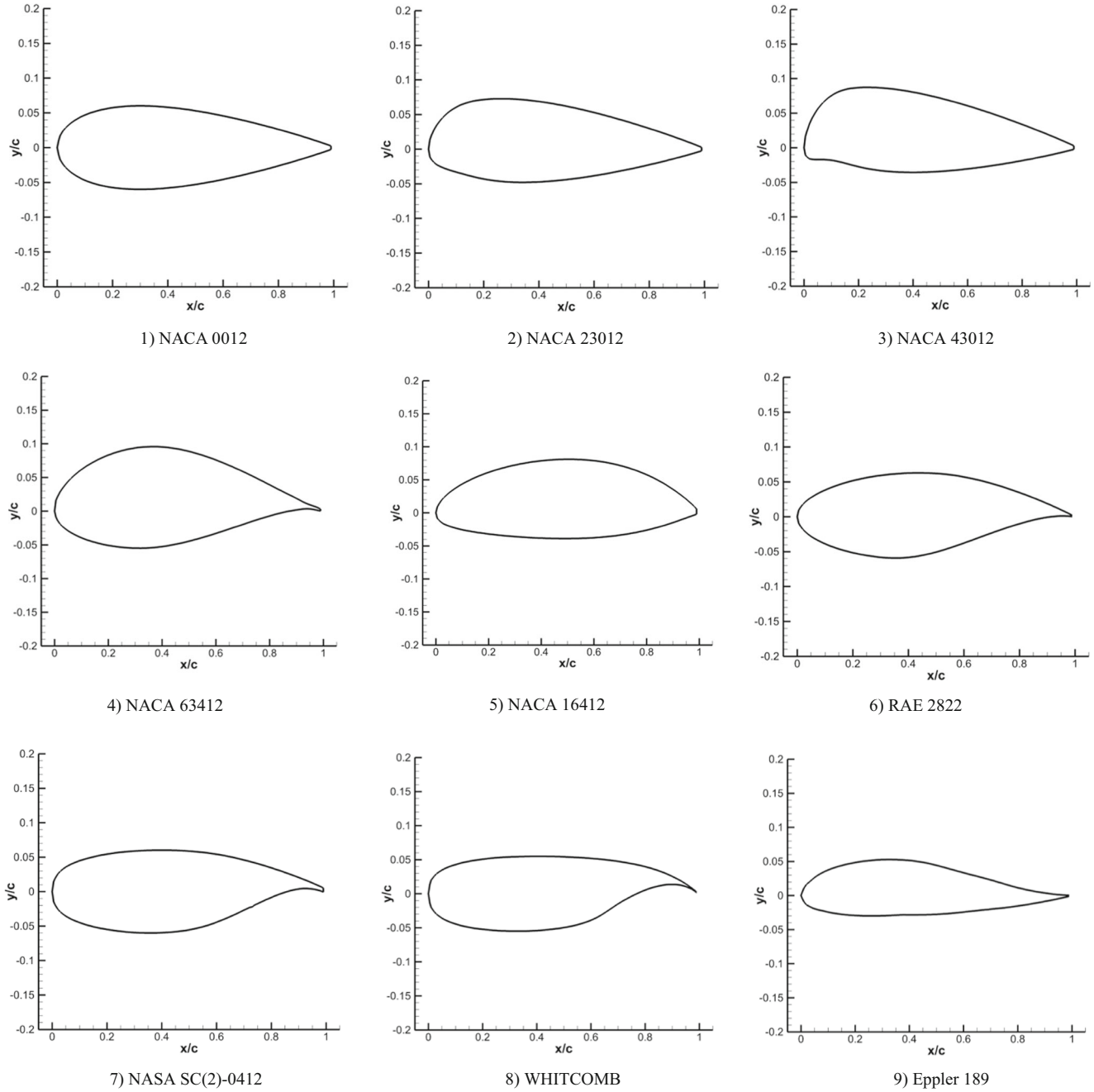

Fig. 12 Shapes of basis hydrofoils

The results are shown in Fig. 10. Compared to the mathematical examples, the engineering application is more complicated, in which MFM is necessary. However, each MFM has its merits and defects. To choose a proper MFM in the shape design optimization, a comprehensive discussion is presented.

(1) For CC1, instead of HF data, the predictive results have the same trend as LF data, which reveals that ignoring the influence on the flow distribution indeed causes errors.

(2) For CC2, though LF and HF data have a big difference, MFM is precise. Besides, CC2 is the fastest one owing to the reduction of computational budgets in LL.

(3) For CC3, due to the inclusion of CC1 in LL, CC3 and CC1 have same HF and LF data. The predictive results show a very good agreement with HF data, but CC3 cost a lot.

(4) In Fig. 10 (4), CC1 and CC3 have slightly better HF data than CC2, which can be explained by the fact that accurate LL result helps to find a right optimization direction.

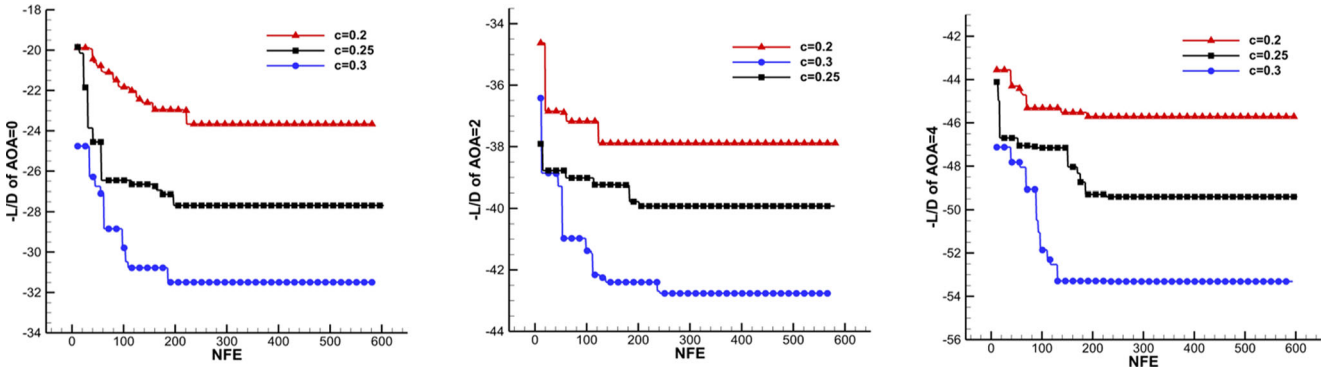

a) AOA=0º b) AOA=2º c) AOA=4º

Fig. 13 Convergence processes of the 2D hydrofoil optimization tests. **a** AOA = 0º. **b** AOA = 2º. **c** AOA = 4º

(5) To compare CC1, CC2, and CC3 more quantitatively, six indices are introduced: (1) The mean of differences between MFM and HF data, (2) the variance of the differences, (3) the mean of HF data, (4) the optimum HF value, (5) the HF response value at the optimum solution of MFM, and (6) the costing time. The first two indices are the error and the trend between MFM and HF responses, respectively. The third index refers to LL optimization abilities, which can provide better UWs under a same condition. The fourth denotes the potential of UL, whereas the fifth represents MFM optimization capability. The last one reflects the computational cost. The indices and their normalized values are listed in Table 2, and the radar diagram is shown as Fig. 11. Besides, the smaller all the indices are, the better the performance MFM has. It is easy to find that CC2 has the best performance.

4 Applications on underwater wing design

4.1 The UL optimization model

Shape parameterization method is a crucial part of UWs optimization, which determines the design variable number and the design space, and it also influences the optimum

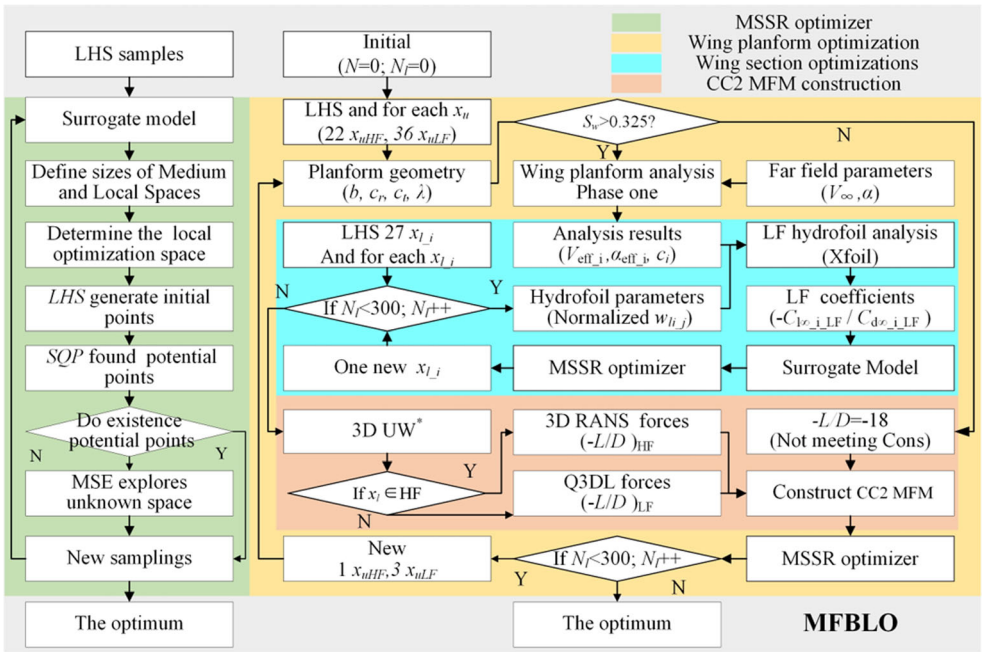

Fig. 14 Flowchart of MFBLO process

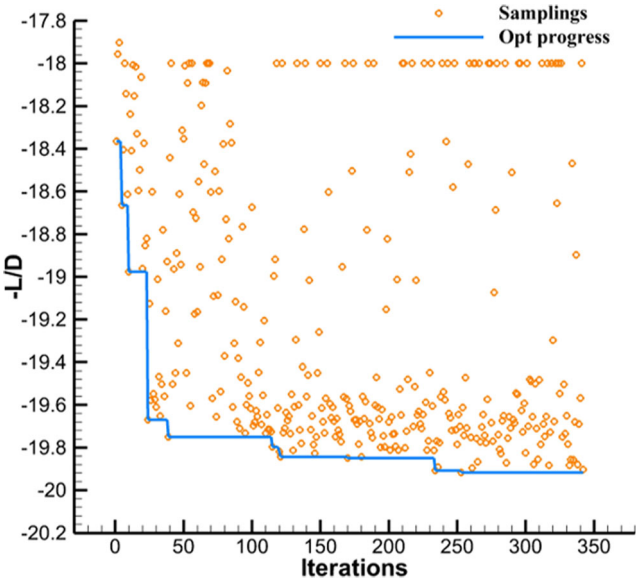

Fig. 15 Optimization process of MFBLO

(Masters et al. 2017). For the UL optimization, the planform geometry is simple and can be directly gained by the inputs listed in Table 1 and Fig. 1. The relative thickness t/c is set as 0.1 to fit the thin hydrofoil theory. The section number ns is set to 8, and thereby the span-wise positions Sp_i are determined as [0, 0.1429, 0.2587, 0.4286, 0.5714, 0.7143, 0.8571, 1]·$b/2$. Hence, the wing span b, the wing root c_r, the wing tip c_t, and the leading edge angle λ are chosen as the UL design variables. Besides, the planform area S_w should not be too small to have good bearing capacity. Thus, a constraint about the planform area that is larger than a given value is introduced. Additionally, the optimal conditions of corresponding LL problems are set up as the constraints to obtain IVs*. The maximum L/D of the UW is considered as the objective function and the UL optimization model as the following:

$$\begin{aligned} &Max && L/D = F_u\left(x_u, IVs^*(x_u, x_l)\right); \\ &working\ conditions: && (\alpha = 4^\circ, t/c = 0.1, v = 1m/s); \\ &W.r.t && c_r/m \quad [0.2, 0.3]; \quad b/m \quad [0.8, 1.6]; \\ & && \lambda/^\circ \quad [0, 40]; \quad c_t/m \quad [0.05, 0.2]; \\ &S.t && S_w > 0.325; \quad x_l \in \underset{x_l \in X_L}{\operatorname{argmin}} \{ f_l(x_u, x_l) \}; \end{aligned} \tag{23}$$

4.2 The LL optimization model

For the parameterized method of hydrofoil shapes, the reduced-basis concept method is adopted (Vanderplaats 1984). In this paper, nine hydrofoils that are analyzed and wind-tunnel tested are selected as the basis hydrofoils, as shown in Fig. 12. Besides, the class and shape function transformation method models the expressions of the basis hydrofoils for the CFD mesh generator (Kulfan 2008). Subsequently, coordinates of the new hydrofoil are provided by the weighted average of the new expression. To match sizes of the control sections, two scaling factors that adjust the chord and the maximum thickness are added in the parameterized method. In conclusion, nine weight coefficients w_{li_j} and two scaling factors totaling 11 inputs are needed to generate a hydrofoil shape. Among them, the weight coefficients are selected as the LL design variables, and the scaling factors are obtained from the UL optimization, which are constraints in the LL optimization. The LL optimization model is expressed as the following:

$$\begin{aligned} &Max && f_{l\_i} = C_{l\infty\_i}(x_{l\_i}) / C_{d\infty\_i}(x_{l\_i}); \\ &working\ conditions: && effective\ incoming\ flow; \\ &W.r.t && w_{li\_j} \in [0, 1]; i = 1, 2...8; j = 1, 2...9; \\ &S.t && \sum_{j=1}^{9} w_{li\_j} = 1; \\ & && scal_{1\_i} = c_i; scal_{2\_i} = thick_i; \end{aligned} \tag{24}$$

4.3 Optimizers

Multi-start space reduction (MSSR) algorithm that is a recently presented surrogate-based global optimization algorithm (Dong et al. 2016) is used as optimizer for UL and LL. Moreover, some modifications like constraints handling and surrogate modeling are added in the both level applications.

MSSR defines three continuously updated design spaces, including global space, medium space, and local space. Meanwhile, a constantly regenerated kriging SM is also constructed to reduce the cost. MSSR alternately chooses the three spaces and employs the multi-start SQP algorithm to find some local optima on kriging. Thereafter, the most potential locations are chosen as supplementary points to update kriging and the design space. Once the multi-start SQP converges to a same point or there are no suitable points in space, the estimated mean square error (MSE) of kriging will be maximized to explore unknown space. The algorithm will continue until the convergence conditions are met.

For the UL optimization, kriging is replaced by CC2. According to the $5n + 2$, $8n + 4$ rule, the initial sampling amount of HF and LF data are 22 and 36, respectively. Besides, an IF condition is set up to eliminate the infeasible solutions before running the simulation for L/D, and the response value of these infeasible solutions is defined as 18. MSSR usually converges on four dimensional mathematical problems within 200 function evaluations. Therefore, the UL termination condition is set as 300 (3D RANS) simulation evaluations.

Table 3 Hydrodynamics and geometries of the application UWs

Results of MFBLO and wing planform optimization (comparison with single-level optimization)						
Hydrodynamics and geometries of the referenced UW (wing planform optimization)						
The response L/D		The wing planform geometry x (optimized)			8-section shape parameters (fixed)	
HF	18.9023 (0.4064/0.0215)	[0.2570, 0.8000 4.1549, 0.1499]			$[1/9]^{8\times9}$	
Area constraint	S_w	0.3255		Normalized constraints	$\sum w_{li\_j}$	$[1]^{8\times1}$
Hydrodynamics and geometries of MFBLO UW (|19.9180–18.9023|/18.9023 = 5.38% improvement than the referenced UW)						
UL results				LL results, section parameter $[x_{l1\_1-9}; x_{l2\_1-9}\ldots;x_{l8\_1-9}]$		
The response L/D		The optimum x_u		[0.0192, 0.1727, 0.2014, 0.3407, 0.0523, 0.0495, 0.0689, 0.0509, 0.0444;		
LF	22.7424 (0.4503/0.0198)	c_r/m	0.3000	0.0119, 0.0609, 0.3955, 0.1997, 0.0945, 0.1039, 0.0565, 0.0394, 0.0378;		
HF	19.9180 (0.4255/0.0213)	$b/2/m$	0.8000	0.0879, 0.0354, 0.2339, 0.3795, 0.0588, 0.0874, 0.0273, 0.0621, 0.0276;		
MFM	19.9192	$\lambda/°$	8.6058	0.0176, 0.0704, 0.2759, 0.1560, 0.1098, 0.2099, 0.0160, 0.0140, 0.1304;		
MFM error	6.3×10^{-5}	c_t/m	0.1095	0.0485, 0.0256, 0.2820, 0.3464, 0.1842, 0.0319, 0.0083, 0.0156, 0.0575;		
				0.0374, 0.0056, 0.2457, 0.2517, 0.2197, 0.0228, 0.0172, 0.0094, 0.1904;		
				0.0144, 0.0647, 0.1870, 0.1870, 0.1655, 0.0576, 0.0935, 0.0288, 0.2014;		
				0.0082, 0.0191, 0.1257, 0.1341, 0.2044, 0.1033, 0.1599, 0.1887, 0.0566]		
Area constraint	S_w	0.3276		Normalized constraints	$\sum w_{li\_j}$	$[1]^{8\times1}$
Results of GWO and EGO (comparison with typical approaches)						
Hydrodynamics and geometries of GWO UW (|19.6136–19.9180|/19.6136 = 1.55% worse than MFBLO UW)						
UL results				LL results, section parameter $[x_{l1\_1-9}; x_{l2\_1-9}\ldots;x_{l8\_1-9}]$		
The response L/D		The optimum x_u		[0.3331, 0.1401, 0.1326, 0.0000, 0.0226, 0.0755, 0.00000, 0.2370, 0.0591;		
LF	–	c_r/m	0.3000	0.0000, 0.3243, 0.0000, 0.0047, 0.0408, 0.0036, 0.2133, 0.2081, 0.2052;		
		$b/2/m$	0.8000	0.0168, 0.0516, 0.1028, 0.0158, 0.0978, 0.2217, 0.0189, 0.4724, 0.0022;		
HF	19.6136 (0.4315/0.0220)	$\lambda/°$	0.2635	0.0552, 0.1723, 0.0271, 0.3635, 0.0346, 0.0002, 0.1187, 0.1620, 0.0665;		
		c_t/m	0.1070	0.0345, 0.0473, 0.0363, 0.3077, 0.0387, 0.0009, 0.2531, 0.2673, 0.0141;		
				0.0421, 0.1414, 0.2525, 0.0719, 0.3086, 0.0812, 0.0000, 0.0703, 0.0320;		
				0.0154, 0.0000, 0.0946, 0.0170, 0.1778, 0.0254, 0.2125, 0.0230, 0.4344;		
				0.0779, 0.1687, 0.2383, 0.0002, 0.1746, 0.1157, 0.1354, 0.0734, 0.0158]		
Area constraint	S_w	0.3256		Normalized constraints	$\sum w_{li\_j}$	$[1]^{8\times1}$
Hydrodynamics and geometries of EGO UW (|19.4960–19.9180|/19.4960 = 2.16% worse than MFBLO UW)						
UL results				LL results, section parameter $[x_{l1\_1-9}; x_{l2\_1-9}\ldots;x_{l8\_1-9}]$		
The response L/D		The optimum x_u		[0.1444, 0.0634, 0.1369, 0.0960, 0.0990, 0.0461, 0.1505, 0.1184, 0.1455;		
LF	–	c_r/m	0.3000	0.1150, 0.0516, 0.1085, 0.0643, 0.1653, 0.0669, 0.1473, 0.1186, 0.1625;		
		$b/2/m$	0.7983	0.1472, 0.1339, 0.0896, 0.1564, 0.1068, 0.1384, 0.0908, 0.0819, 0.0550;		
HF	19.4960 (0.4190/0.02149)	$\lambda/°$	13.4137	0.1268, 0.0706, 0.1847, 0.0984, 0.1353, 0.1592, 0.0400, 0.0841, 0.1010;		
		c_t/m	0.1084	0.0921, 0.1706, 0.1408, 0.0654, 0.1339, 0.0568, 0.1454, 0.1028, 0.0921;		
				0.1047, 0.0811, 0.1628, 0.1771, 0.0780, 0.1711, 0.1305, 0.0687, 0.0260;		
				0.0906, 0.1005, 0.0734, 0.0410, 0.0720, 0.2170, 0.1262, 0.1804, 0.0988;		
				0.1286, 0.1085, 0.1135, 0.1046, 0.1443, 0.0999, 0.1315, 0.1015, 0.0677]		
Area constraint	S_w	0.3260		Normalized constraints	$\sum w_{li\_j}$	$[1]^{8\times1}$
Results of EXP1 and EXP2 (Comparison with LF Optimizations)						
Hydrodynamics and geometries of EXP1 UW (|19.5063–19.9180|/19.5063 = 2.11% worse than MFBLO UW)						
UL results				LL results, section parameter $[x_{l1\_1-9}; x_{l2\_1-9}\ldots;x_{l8\_1-9}]$		
The response L/D		The optimum x_u		[0.0062, 0.1514, 0.1667, 0.2093, 0.2665, 0.0437, 0.0054, 0.1248, 0.0259		
LF	24.5274 (0.4930/0.0201)	c_r/m	0.3000	0.0119, 0.0058, 0.3149, 0.4251, 0.1843, 0.0071, 0.0062, 0.0188, 0.0259		
		$b/2/m$	0.7996	0.0247, 0.0422, 0.2865, 0.3620, 0.2075, 0.0319, 0.0190, 0.0103, 0.0159		
HF	19.5063 (4.2793/2.1938)	$\lambda/°$	5.2426	0.0047, 0.0461, 0.3647, 0.3663, 0.0554, 0.0251, 0.0930, 0.0006, 0.0441		
		c_t/m	0.1145	0.0736, 0.0509, 0.2033, 0.1714, 0.2135, 0.1692, 0.0000, 0.0149, 0.1032		
				0.0147, 0.1159, 0.2060, 0.4177, 0.1380, 0.0326, 0.0334, 0.0113, 0.0304		
				0.0294, 0.0689, 0.1314, 0.2421, 0.2792, 0.1095, 0.0173, 0.0382, 0.0840		
				0.0322, 0.0309, 0.0234, 0.2093, 0.1605, 0.1420, 0.1350, 0.2133, 0.0533]		
Area constraint	S_w	0.3314		Normalized constraints	$\sum w_{li\_j}$	$[1]^{8\times1}$
Hydrodynamics and geometries of EXP2 UW (|18.7655–19.9180|/18.7655 = 6.14% worse than MFBLO UW)						
UL results				LL results, section parameter $[x_{l1\_1-9}; x_{l2\_1-9}\ldots;x_{l8\_1-9}]$		
The response L/D		The optimum x_u		[0.0000, 0.6539, 0.0000, 0.3327, 0.0000, 0.0073, 0.0000, 0.0000, 0.0060;		
LF	22.4129 (0.4505/0.0201)	c_r/m	0.3000	0.3478, 0.0000, 0.0000, 0.3913, 0.0000, 0.1539, 0.0622, 0.0381, 0.0066;		
		$b/2/m$	0.7947	0.0000, 0.0000, 0.0000, 0.1681, 0.8312, 0.0007, 0.0000, 0.0000, 0.0000;		
HF	18.7655 (0.4241/0.0226)	$\lambda/°$	2.2332	0.0003, 0.0000, 0.0592, 0.3173, 0.0909, 0.1166, 0.4119, 0.0000, 0.0037;		
		c_t/m	0.1094	0.1202, 0.3551, 0.0118, 0.0000, 0.0000, 0.0512, 0.4618, 0.0000, 0.0000;		
				0.4080, 0.0000, 0.4080, 0.0001, 0.0000, 0.1684, 0.0000, 0.0155, 0.0000;		
				0.0089, 0.0012, 0.0030, 0.0000, 0.0000, 0.0000, 0.0110, 0.9758, 0.0000;		
				0.0054, 0.0000, 0.0031, 0.0000, 0.0009, 0.9467, 0.0000, 0.0438, 0.0000]		
Area constraint	S_w	0.3254		Normalized constraints	$\sum w_{li\_j}$	$[1]^{8\times1}$

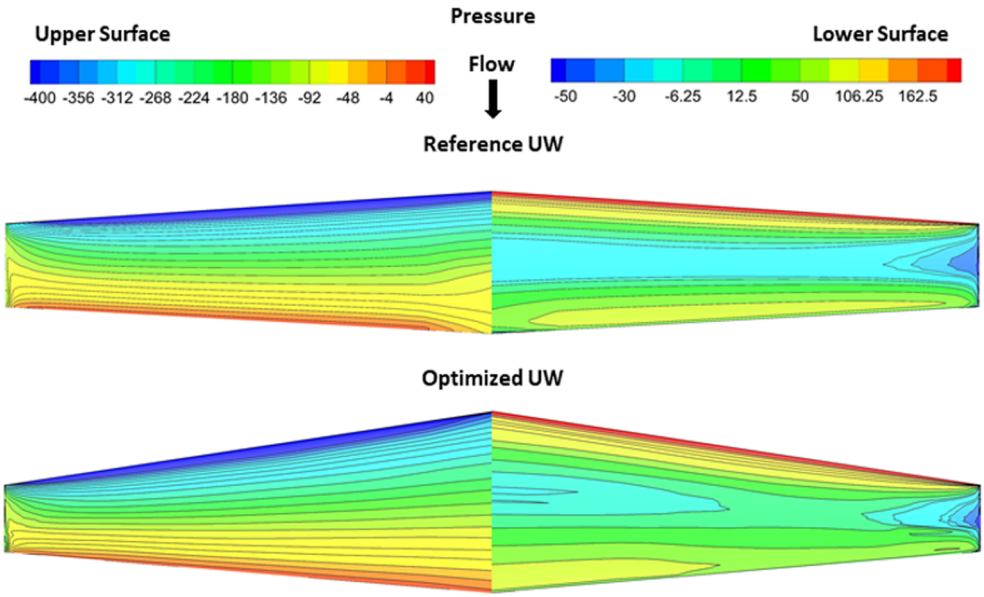

Fig. 16 Pressure counters and planform geometries

For the LL optimization, each task has one kriging model. What is more, four additional parameters including chord, thickness, speed, and AOA are needed. Besides, the design variables are 9 weighted coefficients, the sum of which equals to 1. However, it is almost impossible to satisfy the equality constraint in a 9-dimensional problem due to the huge design space. Hence, the design variables are normalized after each sampling. For the constraints about the chord and the thickness, they are gained by the UL design variables and are directly used in the hydrofoil geometric model.

Considering that the LL iteration number affects the UL optimization, several hydrofoils with different chords and under different AOAs are optimized using MSSR, and the convergence processes of the tests are shown in Fig. 13. Obviously, 300 iterations are good enough for MSSR in the LL optimization. The total flowchart of MFBLO is presented in Fig. 14.

4.4 Result and discussion

HF samples are recorded to describe the convergence process, and the present best values are extracted to plot the iterative curve in Fig. 15. In total, 342 HF samples are obtained, indicating that there are 42 infeasible planform geometries. Besides, the response values locate at [17.8, 19.9], and it is easy to find that the first 22 HF samples generated by LHS are poor (mostly less than 18.5). As the iteration number increases, larger L/D are gradually caputred, proving the effectiveness of the proposed algorithm. Finally, the optimum is found at the 253th iteration, and its response and solution are shown in Table 3. The relative error of HF and MFM response values at optimum point is 6.3×10^{-5}, which demonstrates that the MFM will become more and more precise as the iteration proceeds.

4.4.1 Comparison with single-level optimizations

In Fig. 15, each point involves a single-level optimization loop for the optimal section shapes. Hence, the objective function values of these points in Fig. 15 are always better than those without optimization. Besides, the planform optimization with fixed section parameters needs to be introduced for comparison. Thus, the results of the planform optimization are selected as the referenced UW, listed in Table 3. The bi-level optimization result still has 5.38% improvements than that of the wing planform optimization. Thus, it is necessary to carry out the bi-level optimization to improve the performance. The optimal planform and sections, the corresponding pressure contour, as well as the referenced UWs are shown in Figs. 16 and 17.

Some conclusions in this part can be drawn as follows:

- The planform optimization with sections fixed tends to maximize the aspect ratio to reduce the effect of wing-tip vortices. Nevertheless, the bi-level optimization only attempts to extend the wing spanwise and change shapes of sections, which indicates that the chord is not the most important factor affecting the vortices.
- Due to the strict restriction of section sizes, there is little difference in the section shapes of the referenced and optimized UWs. However, the small perturbations of these shapes have a great impact on the overall fluid performance of the UW.
- The optimized UW has a larger planform area than the referenced case. Hence, the optimized UW has a better bearing capacity. Besides, the optimized UW has a better performance accroding to the pressure

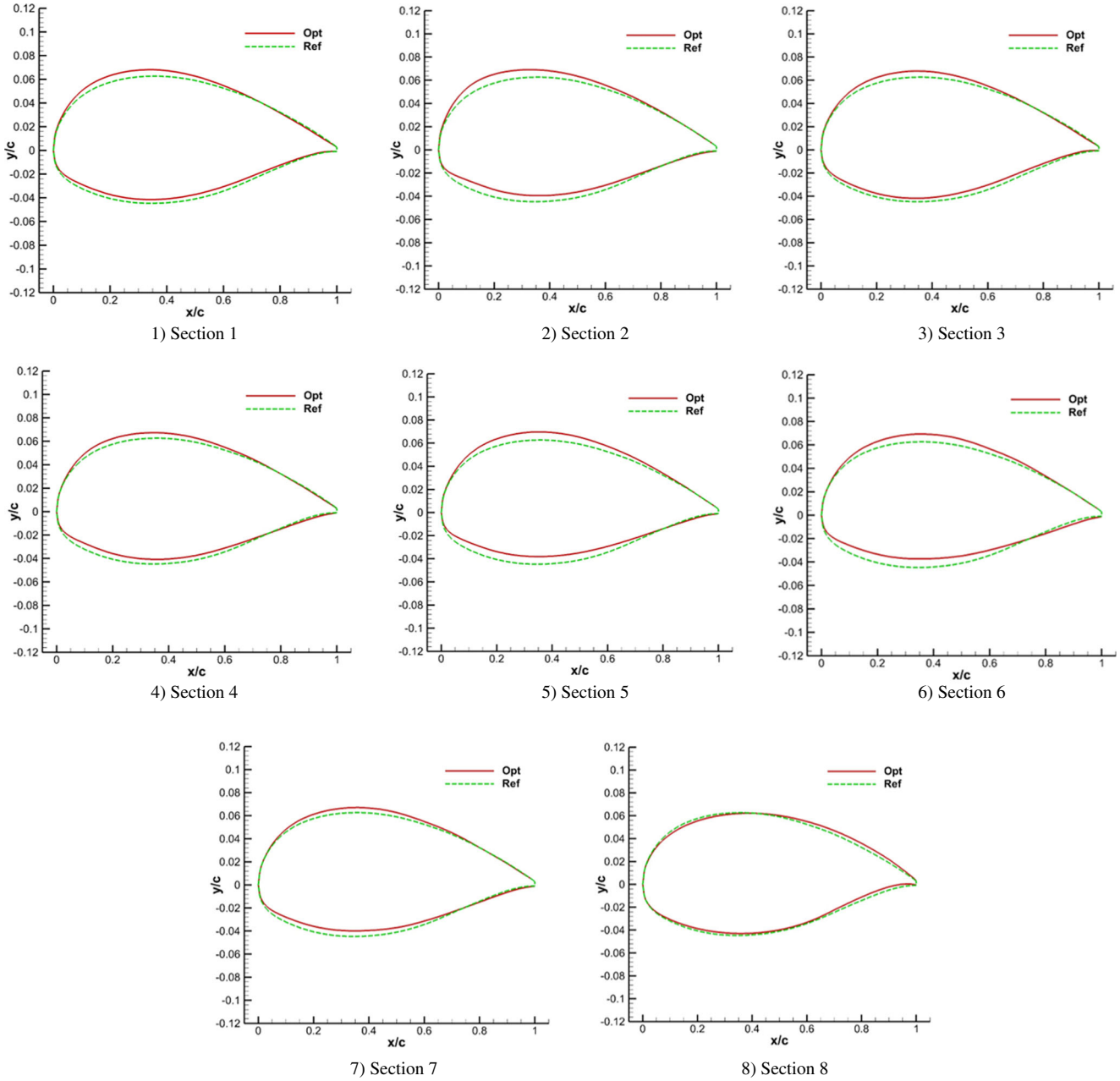

Fig. 17 Shapes of the referenced and optimized sections

contour. For the upper surface contour, the leading edge low-pressure areas of the optimized UW is lager than that of the referenced case, which can imporve the lift. Moreover, the the optimized UW has a more uniform and smooth pressure distribution, and the equivalent lines are almost parallel. For the lower surface contour, fixed section shapes provide a more smooth pressure distribution for the referenced UW. However, multiple section shapes provide a smaller vortex for the optimized UW, according to the wing-tip low-pressure area. A smaller vortex can improve the lift and reduce the induced drag of the UW.

4.4.2 Comparison with typical approaches

Nowadays, approaches of hydrodynamic shape optimizations can be classified into three categories: gradient-based methods, heuristic algorithm assistant methods, and surrogate-based optimizations (Liu et al. 2017). The gradient-based methods are usually very effective, but the solution optimality can be sensitive to the initial guesses and the method often becomes trapped into a local minimum (Chernukhin and Zingg 2013). Thus, to show the advantages of MFBLO, representative approaches in the other two categories that are global optimizations are

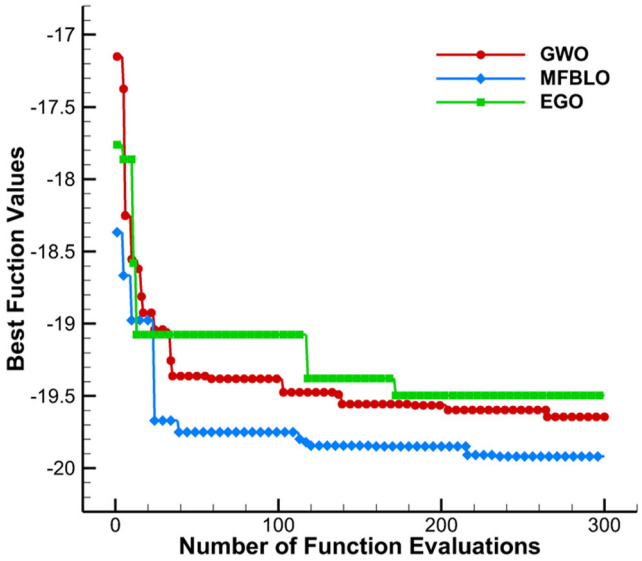

Fig. 18 Convergence curves of MFBLO, GWO, and EGO

chose to design UWs for comparison, including grey wolf optimization (GWO) (Mirjalili et al. 2014) and efficient global optimization (EGO) (Jones et al. 1998). The optimization model is expressed in (25), which keeps same working conditions and design requirements with MFBLO. Besides, all the objective functions are evaluated by RANS simulations. Same as MFBLO, the two approaches also utilize 300 function evaluations as the termination criterion.

$$\begin{aligned}
&\text{Max} \quad L/D;\\
&\text{working conditions}: (\alpha = 4^{\circ}, t/c = 0.1, v = 1m/s);\\
&\text{W.r.t} \quad c_r/m \quad [0.2, 0.3]; \quad b/m \quad [0.8, 1.6];\\
&\qquad \lambda/^{\circ} \quad [0, 40]; \quad c_t/m \quad [0.05, 0.2];\\
&\qquad w_{li_j} \quad [0, 1]; \quad i = 1, 2...8; j = 1, 2...9;\\
&\text{S.t} \quad S_w > 0.325; \quad \sum_{j=1}^{9} w_{li_j} = 1;
\end{aligned} \tag{25}$$

The obtained results from the two methods are listed in Table 3. Obviously, MFBLO gets a bigger L/D than the two approaches. Additionally, about 6.3×10^2 and 1.5×10^4 infeasible samples are generated in GWO and EGO, respectively. Thus, the iterative feasible results of the two optimization methods and MFBLO are also provided in Fig. 18. It is clear that MFBLO has the faster convergence rate. EGO performs worse within the first 50 simulation analyses. Moreover, EGO can hardly find a better solution after 200 analyses, whereas GWO can gradually find better solutions as the iteration progresses. In summary, MFBLO outperforms the two methods on the shape optimization of UWs.

4.4.3 Comparison with LF optimizations

To demonstrate the necessity of constructing MFMs, two experiments EXP1 and EXP2 are carried out. EXP1 is LF bi-level optimization, which adopts (23) and (24) as the mathematical model (Elham et al. 2014). EXP2 is LF traditional optimization, which employ (25) as the model. Both of them adopts LF Q3DL solvers to evaluate the L/D. For optimizer, EXP1 takes MSSR in the two levels. For EXP2, SQP is not able for finning a global optimum, whereas surrogate models need more construction time. Considering that the objective function is a computationally efficient problem, GWO is suitable to apply. The termination criteria of EXP1 and EXP2 are 300 function evaluations, and the optimal results are shown in Table 3. It can be easily found that EXP1 and EXP2 have worse performances than the proposed MFBLO, which demonstrates the necessity of constructing MFMs.

For LF results, the optimum of EXP1 is 24.5274, whereas the optimum of EXP2 is 22.4129. Hence, EXP2 is far from reaching the global optimum of the optimization using LF solver. Similarly, unlike the small numerical gap between the MFBLO and the typical approaches, there may be a large quantity of UWs waiting to be found and evaluated in this gap, because the variance of HF is smaller than that of LF. This may bring an additional long calculation time for the typical approaches to achieve the same result of MFBLO strategy.

5 Conclusions and further research

In this paper, the design variables of the UW shape optimization are classified into an outer layer planform vector and several inner layer section vectors. Meanwhile, based on the finite wing phenomenon, hydrodynamics of UWs can be predicted by the Q3D solver, which combines the planform analysis and several section analyses to gain the results. After separating the design variables and hydrodynamic analyses, the UW shape optimization is divided into an UL optimization merely concerning the planform design and several LL optimizations only related to the wing section designs, which can reduce the dimension. However, the bi-level optimization frame also brings new challenges: large numbers of iterations in LL and the precision reduction. Thus, the additive bridge function MFM is introduced to improve the efficiency and accuracy. Subsequently, three multi-fidelity data fusion approaches are presented and tested for comparison. Among them, CC2 has the best performance and is provided for the shape design. Finally, MFBLO is implemented on the UW shape optimization. For LL, 250 function evaluations are required to find the optimal solution;

for UL, the optimum is found at 253th iteration. The L/D optimized by MFBLO has 5.38% improvements than that of the single-level optimization, 1.55% better than that obtained by the traditional high-dimensional method, and 2.11% improvements than that of the LF optimization.

In our further research, it is of great interest to use the proposed MFBLO to optimize blended wing body underwater gilders. Moreover, MFBLO will also be expanded to solve more challenging problems.

6 Replication of results

Pseudocodes are presented in the Supplementary material to help readers understand better, which includes the part of UL Shape Designer (ULSD), Multi-Fidelity Hydrodynamic Solver (MFHS), and LL Shape Designer (LLSD).

Acknowledgments The authors are also grateful to members of the research group for the implementation of some existing multi-fidelity optimization algorithms.

Funding information Supports are from the National Natural Science Foundation of China (Grant No. 51875466 and Grant No. 51805436) and China Postdoctoral Science Foundation (Grant No. 2018M643726).

Compliance with ethical standards

Conflict of interest The authors declare that they have no conflict of interest.

Appendix 1. Four test cases

Two different wing planform shapes, including straight and swept wings, are selected as basic geometries, and Table 4 lists the parameters. Besides, two different hydrofoils, including symmetric and cambered sections, are chosen as fundamental profiles, as Fig. 19 shows. By combining them arbitrarily, four different test wings are generated, and Table 4 also gives the nomenclatures of the cases. To simulate actual working condition for the UW, the AOAs are set from 0 to 8 degree, and meanwhile, the far-field velocity is set to 1 m/s.

Table 4 Geometry parameters of wings

	b (mm)	c_r (mm)	c_t (mm)	λ°	t/c
Straight	1000.0	250.0	100.0	11.0	0.1
Swept	1260.0	248.786	64.286	27.0	
Nomenclature		Straight wing		Swept wing	
Symmetric		Case 1		Case 2	
Cambered		Case 3		Case 4	

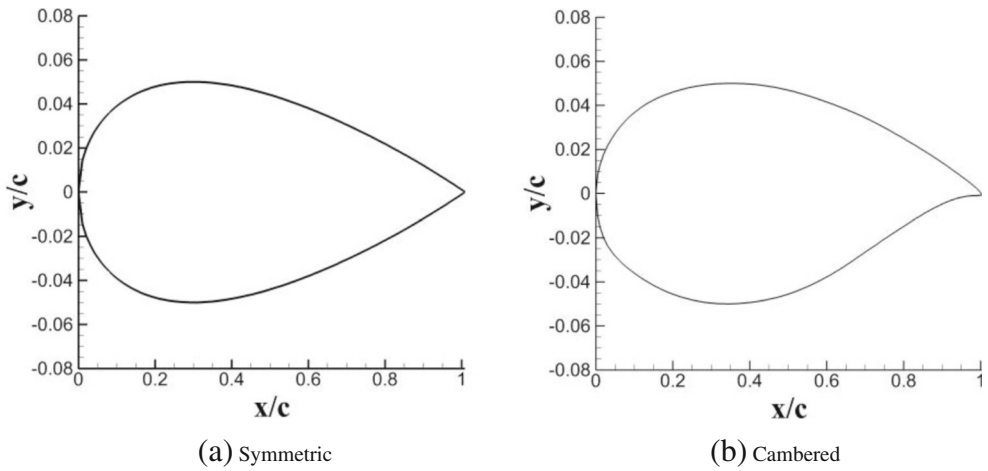

(a) Symmetric (b) Cambered

Fig. 19 Fundamental profile. **a** Symmetric. **b** Cambered

Appendix 2. Five mathematical examples

Table 5 Five MF mathematical examples and their expressions

Formula	Dim	Design space
(1) One-dimensional function: $f(x) = (6x-2)^3 \sin(12x-4)$; $y_h = f(x)$; $y_l = 0.5f(x) + 10(x-0.5) - 5$;	1	$[0, 1]$
(2) Six-hump camel-back function: $f(x_1, x_2) = 4x_1^2 - 2.1x_1^4 + x_1^6/3 + x_1x_2 - 4x_2^2 + 4x_2^4$; $y_h = f(x_1, x_2)$; $y_l = f(0.7x_1, 0.7x_2) + x_1x_2 - 15$;	2	$[-2, 2]^2$
(3) 3D Rosenbrock function: $f(x_1, x_2, x_3) = \sum_{i=1}^{2} \left[100\left(x_i^2 - x_{i+1}\right)^2 + \left(x_i - 1\right)^2\right]$; $y_h = f(x_1, x_2, x_3)$; $y_l = 90\left(x_1^2 - x_2\right)^2 + 1.1(x_3 - 1)^2 + 100\left(x_2^2 - x_3\right)^2 + (x_2 - 1)^2$;	3	$[-2.048, 2.048]^3$
(4) Colville-Himmelblau function: $f(x_1, x_2, x_3, x_4) = 100\left(x_2 - x_1^2\right)^2 + (1 - x_1)^2 + 90\left(x_4 - x_3^2\right)^2 + (1 - x_3)^2$ $+10.1\left((x_2 - 1)^2 + (x_4 - 1)^2\right) + 19.8(x_2 - 1)(x_4 - 1)$; $y_h = f(x_1, x_2, x_3, x_4)$; $y_l = 100\left(x_2 - x_1^2\right)^2 + 1.1(1 - x_1)^2 + 90\left(x_4 - x_3^2\right)^2 + 1.1(1 - x_3)^2$ $+10.1\left((x_2 - 1)^2 + (x_4 - 1)^2\right) + 20(x_2 - 1)(x_4 - 1)$;	4	$[-10, 10]^4$
(5) Hessen function: $f(x_1, ..., x_6) = 25(x_1 - 2)^2 + (x_2 - 2)^2 + (x_3 - 1)^2 + (x_4 - 4)^2 + (x_5 - 1)^2 + (x_6 - 4)^2$; $y_h = f(x_1, ..., x_6)$; $y_l = 0.6f(x_1, ..., x_6) + 0.25(x_2 - 2)^2 + 0.75(x_4 - 4)^2$;	6	$[0, 10]^6$

Appendix 3. Validation of Q3DL, Q3D, and RANS simulations

The simulation results need to be validated with the experiment results to ensure the accuracy. Hence, we adopt experiment results of "Type I-SS" UW, which are tested by Zarruk et al. (2014) in a water tunnel at University of Tasmania. Type I-SS UW is made by stainless steel, whose sections are NACA0009 hydrofoils. Besides, the mesh used for RANS simulation is a structured mesh with 438,870 cells ($y^+ = 5$). The shape and the computational mesh of Type I-SS UW are shown in Fig. 20. The simulation results are shown in Fig. 21. The comparison illustrates that RANS simulation results are in good agreement with the experimental data. Besides, Q3DL and Q3D solvers have the same trend with the experiment data as the angle of attack varies. Thus, RANS is regarded as the highest-fidelity solver, and Q3D is a high-fidelity solver, whereas Q3DL has the lowest fidelity.

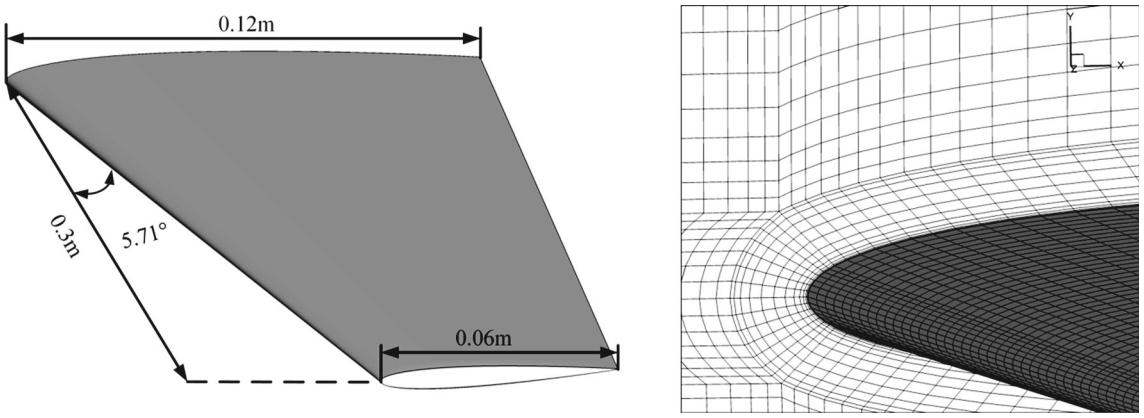

(a) Geometric model of "Type I-SS" UW (b) Detailed meshes of boundary layers

Fig. 20 Shape and computational mesh of "Type I-SS" UW. **a** Geometric model of "Type I-SS" UW. **b** Detailed meshes of boundary layers

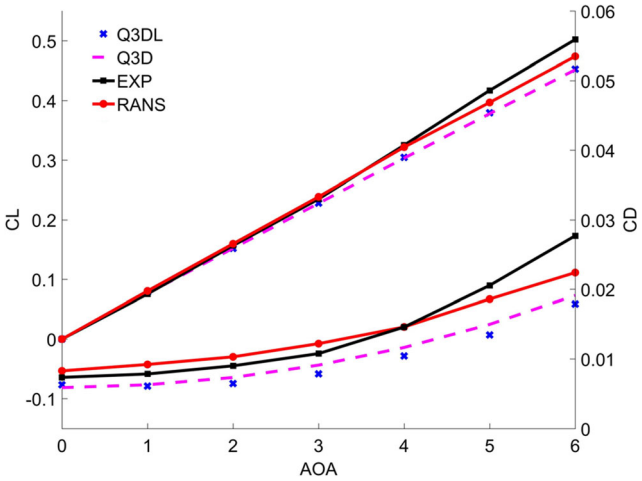

Fig. 21 Simulation results of Q3DL, Q3D, RANS, and experiment

To make sure the simulation results are independent to mesh size, simulated results with different mesh sizes and y + values are compared. The mesh with the sizes 2,205,450 ($y^+ = 0.5$), 1,141,380 ($y^+ = 1$) and 438,870 cells ($y^+ = 5$) are used for simulating the hydrodynamic performance of Type I-SS UW, respectively. Besides, Reynolds number and AOA is set to 1.0×10^6 and 4 degrees, respectively. The results shown in Table 6 indicate that C_L and C_D are almost the same between the finest and coarsest mesh. There are 0.18% and 1.7% differences in C_L and C_D. Hence, compromising between the efficiency and accuracy, the mesh with the sizes 438,870 cells ($y^+ = 5$) are used in this paper.

Table 6 Validation of mesh independence

Mesh size	y^+	C_L	C_D
438,870	5	0.3186	0.0146
1,141,380	1	0.3190	0.0144
2,205,450	0.5	0.3192	0.0143

References

Bohn B, Garcke J, Griebel M (2016) A sparse grid based method for generative dimensionality reduction of high-dimensional data. J Comput Phys 309:1–17

Chernukhin O, Zingg DW (2013) Multimodality and global optimization in aerodynamic design. AIAA J 51(6):1342–1354

Choi S, Alonso JJ, Kroo IM, Wintzer M (2004) Multi-fidelity design optimization of low-boom supersonic business jets, 45th AIAA/ASME/ASCE/AHS/ASC Structures, Structural Dynamics and Materials Conference, Palm Springs, CA, AIAA Paper 2004-1530

Dong H, Song B, Dong Z, Wang P (2016) Multi-start space reduction (mssr) surrogate-based global optimization method. Struct Multidiscip Optim 54(4):1–20

Drela M (1989) XFoil: an analysis and design system for low Reynolds number airfoils. In: Conference on low Reynolds number airfoil aerodynamics. University of Notre Dame, Notre Dame, Indiana

Drela M, Giles MB (1987) Viscous-inviscid analysis of transonic and low Reynolds number airfoils. Am Inst Aeronaut Astronaut J 25(10): 1347–1355

Elham A, Tooren MJLV, Sobieszczanski-Sobieski J (2014) Bilevel optimization strategy for aircraft wing design using parallel computing. AIAA J 52(8):1770–1783

Graf K, Hoeve AV, Watin S (2014) Comparison of full 3d-rans simulations with 2d-rans/lifting line method calculations for the flow analysis of rigid wings for high performance multihulls. Ocean Eng 90: 49–61

Harada T et al (2006) Screening parameters of pulmonary and cardiovascular integrated model with sensitivity analysis. In: Proceedings of the 28th IEEE EMBS Annual International Conference, New York City, USA, 30 Aug–3 Sept 2006

Harrington HA, Gorder RAV (2015) Reduction of dimension for nonlinear dynamical systems. Nonlinear Dyn 88:1), 1–1),20

Hartwig L, Bestle D (2017) Compressor blade design for stationary gas turbines using dimension reduced surrogate modeling. Evolutionary Computation. IEEE, pp 1595–1602

Huang E, Xu J, Zhang S, Chen C-H (2015) Multi-fidelity model integration for engineering design. Proc Comput Sci 44:336–344

Islam MM, Singh HK, Ray T (2017) A surrogate assisted approach for single-objective bi-level optimization. IEEE Trans Evol Comput (99):1–1

Javaid MY, Ovinis M, Nagarajan T, Hashim FBM (2014) Underwater gliders: a review, vol 13. EDP Sciences, p 02020

Jeroslow RG (1985) The polynomial hierarchy and a simple model for competitive analysis. Math Program 32(2):146–164

Jones DR, Schonlau M, Welch WJ (1998) Efficient global optimization of expensive black-box functions. J Glob Optim 13(4):455–492

Koch PN, Simpson TW, Allen JK, Mistree F (1999) Statistical approximations for multidisciplinary design optimization: the problem of the size. J Aircr 36(1):275–286

Koo D, Zingg DW (2017) Investigation into aerodynamic shape optimization of planar and nonplanar wings. AIAA J 56:1), 1–1),14

Kulfan BM (2008) Universal parametric geometry representation method. J Aircr 45(1):142–158. https://doi.org/10.2514/1.29958

Leifsson L, Koziel S (2015) Aerodynamic shape optimization by variable-fidelity computational fluid dynamics models: a review of recent progress. J Comput Sci 10:45–54

Li J, Chen JB (2006) The dimension-reduction strategy via mapping for probability density evolution analysis of nonlinear stochastic systems. Probab Eng Mech 21(4):442–453

Li C, Wang P, Dong H (2018) Kriging-based multi-fidelity optimization via information fusion with uncertainty. J Mech Sci Technol 32(1): 245–259

Liu J, Song WP, Han ZH, Zhang Y (2017) Efficient aerodynamic shape optimization of transonic wings using a parallel infilling strategy and surrogate models. Struct Multidiscip Optim 55(3):925–943

Luo W, Lyu W (2015) An application of multidisciplinary design optimization to the hydrodynamic performances of underwater robots. Ocean Eng 104(23):686–697

Lyu Z, Kenway GKW, Martins JRRA (2014) Aerodynamic shape optimization investigations of the common research model wing benchmark. AIAA J 53(4):968–985

Mariens J, Elham A, Tooren MJLV (2014) Quasi-three-dimensional aerodynamic solver for multidisciplinary design optimization of lifting surfaces. J Aircr 51(2):547–558

Masters DA, Taylor NJ, Rendall TCS, Allen CB, Poole DJ (2017) Geometric comparison of aerofoil shape parameterization methods. AIAA J 55(5):1575–1589. https://doi.org/10.2514/1.J054943

Mei Y, Omidvar MN, Li X, Yao X (2016) A competitive divide-and-conquer algorithm for unconstrained large-scale black-box optimization. ACM Trans Math Softw 42(2):13

Mirjalili S, Mirjalili SM, Lewis A (2014) Grey wolf optimizer. Adv Eng Softw 69(3):46–61

Mitsos A, Chachuat B, Barton PI (2009) Towards global bilevel dynamic optimization. J Glob Optim 45(1):63

Molland AF, Bahaj AS, Chaplin JR, Batten WMJ (2004) Measurements and predictions of forces, pressures and cavitation on 2-d sections suitable for marine current turbines. Proc Inst Mech Eng M 218(2): 127–138

Moritz S, Oliver PC, Kilian O (2016) Spectral proper orthogonal decomposition. J Fluid Mech 792(7):798–828

Nguyen NV, Choi SM, Kim WS, Lee JW, Kim S, Neufeld D et al (2013) Multidisciplinary unmanned combat air vehicle system design using multi-fidelity model. Aerosp Sci Technol 26(1):200–210

Oberkampf WL, Trucano TG (2002) Verification and validation in computational fluid dynamics. Adv Mech 38(3):209–272

Quashie M, Marnay C, Bouffard F, Joós G (2018) Optimal planning of microgrid power and operating reserve capacity. Appl Energy 210 pp. 1229–1236. https://doi.org/10.1016/j.apenergy.2017.08.015

Ragon SA, Guacute Z, Haftka r RT, Tzong TJ (2015) Bilevel design of a wing structure using response surfaces. J Aircr 40(5):985–992

Regis RG (2015) Trust regions in surrogate-assisted evolutionary programming for constrained expensive black-box optimization. Infosys Science Foundation, 51–94

Rudnick DL (2016) Ocean research enabled by underwater gliders. Annu Rev Mar Sci 8:519–541. https://doi.org/10.1146/annurev-marine-122414-033913

Shan S, Wang GG (2010) Survey of modeling and optimization strategies to solve high-dimensional design problems with computationally-expensive black-box functions. Struct Multidiscip Optim 41(2): 219–241

Simpson TW, Mauery TM, Korte JJ, Mistree F (2001) Kriging models for global approximation in simulation-based multidisciplinary design optimization. AIAA J 39(12):2233–2241

Sinha A, Malo P, Deb K (2018) A review on bilevel optimization: from classical to evolutionary approaches and applications. IEEE Trans Evol Comput 22(2):276–295

van Ingen JL (2008) The en method for transition prediction. Historical review of work at tu delft. Proceedings of the 38th AIAA fluid dynamics conference and exhibit, Seattle, Washington, June 23-26, 2008, p. 1–49; AIAA paper 2008–3830. https://doi.org/10.2514/6.2008-3830

Vanderplaats GN (1984) Numerical optimization techniques for engineering design: with applications. McGraw-Hill

Viswanath, Asha (2010) Dimension reduction for aerodynamic design optimization. (Doctoral dissertation, University of Southampton)

Wang L, Shan S, Wang GG (2004) Mode-pursuing sampling method for global optimization on expensive black-box functions. Eng Optim 36(4):419–438

Wang X, Chang Y, Zhang P (2018) Traffic signal optimization based on system equilibrium and bi-level multi-objective programming model. In: Wang W, Bengler K, Jiang X (eds) Green intelligent transportation systems. GITSS 2016. Lecture notes in electrical engineering, vol 419. Springer, Singapore. https://doi.org/10.1007/978-981-10-3551-7_34

Yang P, Tang K, Yao X (2018) Turning high-dimensional optimization into computationally expensive optimization. IEEE Trans Evol Comput 22(1):143–156

Yata K, Aoshima M (2010) Effective PCA for high-dimension, low-sample-size data with singular value decomposition of cross data matrix. Academic Press, Inc

Zarruk GA, Brandner PA, Pearce BW, Phillips AW (2014) Experimental study of the steady fluid–structure interaction of flexible hydrofoils. J Fluids Struct 51:326–343

Zhang N (2014) Hilbert-Schmidt independence criterion in sufficient dimension reduction and feature screening. Ph.D. dissertation, Department of Statistics, The University of Georgia, Georgia, Athens, 2014. http://purl.galileo.usg.edu/uga_etd/zhang_nan_201405_phd. Accessed 08 Aug 2019